Technische Universität Berlin
Fakultät I – Sprache und Kommunikation
Audiokommunikation und -technologie

Master's Thesis:

Empirical and Numerical Analysis of Broadband Absorber Traps

Bradley Alexander

Supervision: Prof. Dr. Stefan Weinzierl
Dr. Drasko Masovic

<u>Eidesstattliche Erklärung</u>

Hiermit versichere ich, dass ich die vorliegende Arbeit selbstständig verfasst und keine anderen als die angegebenen Quellen und Hilfsmittel benutzt habe. Alle Ausführungen, die anderen veröffentlichten oder nicht veröffentlichten Schriften wörtlich oder sinngemäß entnommen wurden, habe ich kenntlich gemacht.

Die Arbeit hat in gleicher oder ähnlicher Fassung noch keiner anderen Prüfungsbehörde vorgelegen.

_____ _____

Ort, Datum   Unterschrift

Abstract

The acoustic quality of small to medium size listening or communication rooms generally depends on sufficiently low reverberation times and the proper balance of frequency content at designated listening positions. Achieving this requires the careful consideration of source and receiver positions, room geometry, surface treatments, and the implementation of sound absorbers in the associated frequency ranges. A significant challenge lies in the broadband damping of low frequency room modes which tend to color the frequency response, without overly damping the frequency range containing the most important auditory content. The following study presents an analysis of a broadband absorber trap designed to specifically deal with this problem, providing empirical data on its effectiveness, and an analytical and numerical investigation of its physical damping mechanisms as well as implementation in room simulations using the finite element method. Results of the study show that the absorber module has effective broadband absorption capacity below 400 Hz, reaching peak absorption of $\alpha = 0.89$ at 125 Hz, and moderate absorption above 400 Hz ranging between 0.3 and 0.5, reducing room reverberation times in frequency ranges respective to absorption strength. Additionally, FEM simulations show that specific absorber configurations will significantly reduce the standard deviation of frequency responses over a considerable listening area, which may be adapted according to acoustic room planning strategies.

Zussamenfassung

Die akustische Qualität von kleinen bis mittelgroßen Hör- oder Kommunikationsräumen hängt im Allgemeinen von ausreichend niedrigen Nachhallzeiten und der richtigen Ausgewogenheit des Frequenzgehalts an den vorgesehenen Hörplätzen ab. Um dies zu erreichen, müssen Quell- und Empfängerpositionen, Raumgeometrie, Oberflächenbehandlungen und der Einsatz von Schallabsorbern in den entsprechenden Frequenzbereichen sorgfältig abgewogen werden. Eine bedeutende Herausforderung liegt in der breitbandigen Dämpfung tieffrequenter Raummoden, welche die Neigung aufweisen, den Frequenzgang zu verfärben, ohne jedoch den Frequenzbereich mit den wichtigsten Hörinhalten übermäßig zu dämpfen. Die folgende Studie stellt die Analyse eines Breitband Absorber Traps vor, welches speziell auf dieses Problem ausgerichtet ist. Die Studie liefert empirische Daten zu der Wirksamkeit des Traps, sowie eine analytische und numerische Untersuchung der physikalischen Dämpfungsmechanismen, außerdem wird die Implementierung in Raumsimulationen mit der Finite-Elemente-Methode dargestellt. Die Ergebnisse der Studie zeigen, dass das Absorbermodul unterhalb von 400 Hz ein effektives Breitband-Absorptionsvermögen aufweist und die Nachhallzeiten des Raums in den entsprechenden Frequenzbereichen deutlich reduziert. Bei 125 Hz wird eine maximale Absorption von α = 0,89 erreicht, oberhalb von 400 Hz eine moderate Absorption zwischen 0,3 und 0,5. Darüber hinaus zeigen FEM-Simulationen, dass spezifische Absorberkonfigurationen, die je nach akustischen Raumplanungsstrategien angepasst werden können, die Standardabweichung der Frequenzgänge über einen beträchtlichen Hörbereich verringern.

Acknowledgement

I would like to extend my deep gratitude to Prof. Dr. Weinzierl, Prof. Dr. Fuchs, and Dr. Masovic for the invaluable support and advice given to me throughout and beyond this thesis.

In addition, I would like to thank Nele, my parents, and my grandfather for their encouragement and patience throughout the last few years.

Finally, I dedicate this master's thesis to my son Levi, the reason I went back to school in the first place. I will never forget having to relearn all of high school mathematics in the exhaustive months after you were born.

Table of Contents

List of Figures

1. Introduction

The complex task of characterizing and optimizing the sound field at low frequencies in smaller rooms is a physics problem familiar to room acoustic engineers, whose objective it is to plan or improve the acoustics within an architectural space. Regardless of what method is used, there will always remain a degree of uncertainty inherent to the mathematical predictions or the observational measures used to assess the outcome.

Nevertheless, every case study and methodological improvement is a step towards increased accuracy and ease of prediction, and the task itself is not for naught, leading to a significant amount of research in the past 25 years. Any small to medium sized room in which the transmission, comprehension, and assessment of auditory information plays the most significant role in terms of the architectural program of the space, regardless of whether the content is a recording, live broadcast, or real time music or speech, must be acoustically treated so that the transfer of information from source to receiver sounds as it was intended to. Smaller dimensions of the room increase the prevalence and influence of low frequency room modes, standing sound waves defined and bounded by the enclosure geometry, within the entire space. Since the set of room modes, also known as eigenmodes, are a property of the physical space and its respective boundaries, attempts to equalize their effect on the frequency response at an observation point generally require architectural interventions which include, but are not limited to, the implementation of devices or boundaries designed to damp frequencies with longer wavelengths. Compared to the excitation of a fixed string, a room will resonate at various frequencies depending on how and where it is excited. In order to change the set of frequencies at which a string may be excited, either the mounting conditions, length and width of string, or the material properties of the string must be altered. In the same way, altering the dimensions and surface boundary conditions of a physical space will change the amplitude, frequency, and phase at which resonant frequencies in a specific location within the space may be observed. The reason why controlling this behavior is necessary is simple. Interferences in the sound field within the room caused by standing waves greatly increase or decrease the sound pressure at certain frequency bands cause undesired colorations or distortions to the

transmitted sonic content. Additionally, the failure to attenuate low frequencies of a higher amplitude will result in excessive reverberation times at that frequency band, causing a temporary overlap between reverberation tails and the direct sound or early reflections of later pieces of audio information.

This master's thesis is an analysis of a device and its implementation, designed to deal with exactly the problem described above. The methods used here utilize the findings of researchers over the last decades, and the contribution of this work includes an explanation of the combination of the effective physical damping mechanisms present in a single device which does not alter the exterior boundary geometries and conditions of the space, rather constitutes an array of internal damping volumes within the sound field which effectively attenuate a broadband set of low frequencies. As a result, the standard deviation within the frequency responses decrease at a localized array of observation points within the space, depending on the configuration of the absorber placement. Additionally, this work will discuss the development of a numerical modelling strategy using the finite element method not only for the computation of the necessary surface impedance values needed for the simulation of room frequency responses, but the implementation of the calculated values in the domain and boundary definitions needed to simulate internal damping in a virtual room. The device in question is called the BAT, which stands for Broadband Absorber Trap, which was designed by Prof. Dr. Helmut Fuchs, and implemented and analyzed together with the department of Audio-communication and Technology at the TU Berlin.

Since no simple analytical solution exists for this problem, it has been tackled with various methods from different perspectives, whose issues are discussed in this thesis and concern the following: the empirical, analytical, and numerical methods for finding the surface impedance of a "free-floating" resonance and porous absorber, the verification of its absorption mechanisms and their respective frequency ranges, the numerical simulation of the device in a virtual space, and the quantitative characterization of the effects the device has on a set of frequency responses using statistical methods. The structure of this thesis is to present the research relevant to this study, followed by a description of the methods used for measuring and modelling. The results will then be presented and analyzed, and finally discussed in the concluding chapters.

In 2012 and 2013 two works appeared which seem to have necessitated the developments discussed here. Firstly, the necessity for absorber devices which attenuate low frequencies without overly damping higher frequencies was made explicit in a paper that proposed a novel numerical model for the prediction of reverberation times which take the damping of low frequency room modes into account (Dance and Van Buuren 2013). In the same paper, the development of the covered broadband absorber by Fuchs and Lampert (2013) was mentioned as a device which offers a solution to the problem. More recently however, research has been conducted on the efficiency of acoustic meta-surfaces with profound broadband capabilities in the low frequency range, installed as acoustic paneling in a room (Ji and Li 2020).

While some researchers discussed and admitted the difficulties that arise when measuring the absorptive properties of low frequency absorbers, specifically bass-traps and membrane absorbers (Calder, 2018), considerable work was done to improve the methods used in FEM simulations in the wave theoretical frequency range, though a call was made for improved measurement and simulation techniques for better defining the boundary conditions for such simulations. The focus in this case was on measuring and modelling the surface impedance, which is exactly the property needed for the finite element simulations of acoustic spaces (Aretz 2012). Rindel and colleagues published several papers on the development of optimization (Mondet, Brunskog, Jeong, and Rindel 2017; 2020) and analytical (Rindel 2011) models for estimating the complex pressure reflection factor and the resulting surface impedance of absorber mechanisms based on statistical absorption coefficients, the latter of which were measured in the early stages of this project. In 2015, Rindel published a numerical method for predicting the frequency response and reverberation times for rectangular rooms using calculations based on modal energy analysis (Rindel 2015). Other methods for estimating modal reverberation times of rectangular rooms were developed, for example, by Meissner (2008), who found that the location of modes in a symmetrical room affected the decay time to a greater extent than individual damping factors or room geometry. In contrast, an FEM implementation was used to establish a connection between boundary admittance and modal decay times, whereby boundary admittance directly affects the damping factor of a mode (Magalotti and Cardinali 2019). The same

authors also developed a simple formula based on FEM results for estimating modal decay times, which appears to display good agreement between theoretical and experimental results (Magalotti and Cardinali 2018).

The FEM approach for rectangular rooms is compared with analytical modelling methods, as Prislan, Veble, and Svensek did by implementing the acoustic Green's function with more precise boundary condition definitions, and interestingly, using a ray-tracing model of the function as opposed to a modal model (Prislan, Veble, and Svensek 2016; Prislan and Svensek 2017). In both cases very good agreement was found. Meissner compared an analytical and numerical approache in various papers in which he analyzed the relationship between absorber placement, room geometry, modal density, damping, and reverberation times, finding that irregular room shapes increases modal density, and absorber placement may directly affect the reverberation time of specific frequency bands in irregularly shaped rooms (Meissner 2005; Meissner 2007). Later, in 2018, Meissner also introduced a numerical method for optimizing the frequency response in rooms with various size ratios by observing the minimum standard deviation (Meissner 2018). Both modal spacing and standard deviation are established markers for frequency response optimization, as shown in an empirical study observing subjective perception of single modes with varying Q-factors (Wankling and Fazenda 2008), and the relationship between room dimensions, receiver and source positions, as well as the minimization of frequency response deviation using a numerical procedure (Cox, D'Antonio, and Avis 2004). Another numerical solution designed to solve the eigenfrequency problem in damped rectangular rooms was introduced by Bistafa and Morrissey in 2002 (Bistafa and Morrissey 2002).

The development of the FEM modelling technique for acoustic simulations has been tested and improved over the last 25 years, with innovations addressing various aspects of the procedure. Already in 1997, the technique was discussed as a useful tool for modelling low-frequency sound fields in small rooms (Pietrzyk and Kleiner 1997), though the common laments are the computational costs and limits of what can be practically computed, generally being the overall size of the model and limited frequency range. Most recently, however, researchers have been developing and testing a new FEM solver type, specifically designed to

model plane-wave propagation with coarser meshes and fewer degrees of freedom, which significantly reduces computation time. The finite element method has also been incorporated into a standalone tool for mode shape calculation and SPL variance and distribution, helpful for the analysis of regularly and irregularly shaped rooms (Sevastiadis, Kalliris, and Papanikolaou 2010). Another piece of FEM software was developed for optimizing the frequency responses over a listening area by algorithmically calculating the most ideal characteristics of a covered porous absorber material (Bistafa, Hodgkin, Morita, Köhn, and Neto, 2012). FEM algorithms have also been implemented in MATLAB, as shown in a 2013 paper, in which the horizontal pressure distribution at discrete frequencies in a rectangularly shaped room was visualized, though higher degrees of error were found to be a result of imprecise boundary condition definitions (Peter 2013).

Two papers were found to be very influential for the development of this thesis. The first being an empirical study on the effect of porous absorber placement on the reverberation time, speech transmission index, and early reflection time in a mock classroom (Cucharero, Hänninen, and Loki 2019). In this study, researchers found that the observed acoustic parameters, were improved when porous absorption was not placed in the corners and edges between the ceiling and walls, except when the sound field in the room is dominated by the modal frequency range, in which case absorbers should be placed in locations associated with causing the mode. The statistical nature and frequency range of the study was a further indication that more work needs to be done in clarifying what happens when damping modules with exceptional low frequency capacities are properly measured and modelled and implemented into a numerical method. As the conclusions of some of the mentioned studies state, improvements were necessary for better boundary condition definitions or the necessity for low frequency absorber modules. The second study also used a statistical approach, which has been adopted and modified in this thesis, for examining the change in deviation of room frequency responses over a listening area as a result of porous absorber positioning and surface area (Lau and Powell 2018). Again, here, the absorber modelled in the study had poor low-frequency absorption characteristics, again indicating a void in the current research.

This thesis includes a brief introduction to the BAT and its basic properties. Early reverberation chamber measurements establishing the aequivalent absorption area of individual units and the derived statistical absorption coefficients are then presented, followed by two case-studies of the implementation of the BAT in a real space which correlates the in-situ measurements to the reverberation chamber results. Impedance tube measurements were taken to measure the surface impedance and derived absorption coefficients of the various absorption mechanisms at work in a BAT which was designed with dimensions to exactly fit the tube, and presented here in the study, followed by a presentation of the analytical models used to predict the absorption coefficients. The study introduces the finite element method-based modelling strategy implemented to assess the surface impedance of a BAT whose dimensions are representative of the real physical module. In the results section, the calculations of the model, namely the absorption coefficients and impedances are compared to the results of both the analytical and empirical studies. Its FEM implementation and simulation in a virtual three-dimensional environment will be discussed, which also details the sound field changes resulting from various permutations in absorber placement. The complete set of results from the simulation will be included in an appendix, while the most relevant results will be presented in the results section. A final analysis examines both wave-theoretically and statistically the results of the simulation which appear to correlate with aspects of the results from the studies mentioned in this introduction.

Again, the purpose of this study is to discuss the measurements, mathematical descriptions, and numerical simulations of the physical mechanisms responsible for the absorption characteristics displayed by the broadband absorber trap. The absorption characteristics are then analyzed in terms of their effect on the low-frequency sound field, presented as a set of spatial arrays of frequency responses which vary based on absorber placement. The results and findings are examined both statistically and theoretically. Though the initial hypothesis which initiated this project is quite simple, namely that the BAT is not a simple damped plate resonator, rather a damping device which includes both a plate resonator and porous absorber, this analysis will not only show that the broadband absorber trap does in fact use both physical mechanisms in order to minimize the standard deviation of frequency responses in a room location which can be specifically

16

targeted, but also that the frequency responses display pronounced reductions in low frequency room eigenmode amplitudes and frequency shifts which result in a frequency shift in modal density and allow for improved damping and control of modal behavior in a room.

2. Methods

As previously stated, the methods used in this study include reverberation chamber measurements, in-situ measurements of rooms treated with BAT modules, impedance tube measurements, analytical predictions, and the finite element method. The methods will be presented here, preceded by a brief description of the absorber module.

2.1. Description of the absorber module

The broadband absorber trap as seen in Figure 1 consists of a 30 x 30 x 60 cm steel case completely filled with mineral wool, whose specific fluid resistance is 5 kPa*s/m^2. The steel case consists of two plates each with a thickness of 0.7 mm. The plates are cut and bent to create a case whose sides are fastened with rivets along the overlap. The default module has two large and small sides which are smooth. The two other large sides are perforated with circular holes which have a 1.5 mm diameter, resulting in a plate porosity is 22%. The module is hung from the ceiling via steel cable attached at the four eyelets fixed to the top plate.

Figure 1. An array of broadband absorber traps pictured on the floor of a reverberation chamber

2.2. Measurements in the reverberation chamber

A series of reverberation chamber measurements were conducted to establish the aequivalent absorption area and resulting absorption coefficients. The reverberation chamber measurement method, according to DIN EN ISO 354 – 2003 -12, measures the ability of a material to absorb sound energy by calculating the added absorption when comparing the measured reverberation times of the empty chamber and chamber with absorption units or surfaces, by using the interrupted noise or impulse response method. The added aequivalent absorption area may be found with

$$A_{eq} = 0.163 * V \left(\frac{1}{T_{with}} - \frac{1}{T_0} \right) [\text{m}^2] \qquad (2.2.1)$$

where V is the volume of the chamber in m³;

T_{with} is the reverberation time of the filled chamber in s;

and T_0 is the reverberation time of the empty chamber in s.

The average absorption coefficients can be found with

$$\alpha_{s,ave} = \frac{A_{eq}}{S}. \qquad (2.2.2)$$

The calculation of the absorption coefficients depends on the surface area S of the absorber material. In this study, a variety of absorber module configurations were used to take the measurements, which lead to a change in irradiated surface area. For this reason, it was necessary to calculate the average absorption coefficients relative to the exposed surface area of the specific measurement which resulted in the calculated aequivalent absorption area, which gives the equation

$$\alpha_{s,ave} = \frac{1}{N} \sum_{i=1}^{N} \frac{A_i}{S_i} \qquad (2.2.3)$$
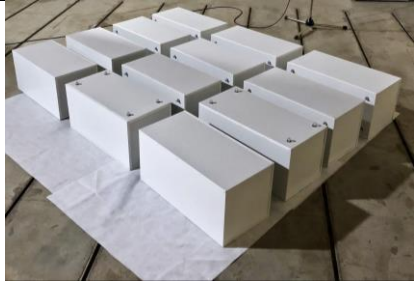
where N is the total number of measurements;

and i is the index of the specific measurement setup.

The absorbers were placed either in the center of the room, with varying gap sizes between absorbers and the floor, as well as in the room edges, with varying

gap sizes between the absorber modules and the wall. Descriptions of the specific measurement setups may be found in Figure 2.

Setup Number	Image	Description; a = distance between modules, h = height from floor.	Total irradiated surface S in m^2
1		a = 100 mm, perforations facing upwards into room, sides unperforated, placed in center of chamber	8.64
2		a = 200 mm, perforations facing upwards into room, sides unperforated, placed in center of chamber	8.64
3		a = 400 mm, perforations facing upwards into room, sides unperforated, placed in center of chamber	8.64
4		a = 100 mm, h = 200 mm, perforations facing upwards into room, sides unperforated, placed in center of chamber	10.8

5		a = 200 mm, h = 200 mm, perforations facing upwards into room, sides unperforated, placed in center of chamber	10.8
6		a = 400 mm, h = 200 mm, perforations facing upwards into room, sides unperforated, placed in center of chamber	10.8
7		a = 200 mm, h = 200 mm, perforated sides to floor and wall, placed in edges of chamber	10.8
8		a = 400 mm, h = 200 mm, perforated sides to floor and wall, placed in edges of chamber	10.8

Figure 2. Descriptions of measurement setups used in reverberation chamber tests

2.3. Implementation of BAT in sample rooms

The effectiveness of the BAT's ability to reduce the reverberation time in a room was tested in two sample rooms. The rooms had slightly different geometries and considerably different volumes, while both consisted of rectangular volumes.

The reverberation times of the *before* and *after* states of each room were measured using the standard measurement procedure described in DIN EN ISO 3382:2:2009 for ordinary rooms, using the interrupted noise method.

The first room to be measured was a small meeting room in a scientific instrument facility, whose volume was 73 m^3. The room was first measured in its empty state (Figure 3) with all possible furniture removed, then treated with 15 BATs which were fixed in the upper edges of the room at a distance of 10 cm from the ceiling as seen in Figure 4.

Figure 3. Ceiling of meeting room before BAT installation

Figure 4. Installation of 15 BATs in meeting room

The second room to be treated was a small classroom in the *Max Dortu School* in Potsdam. The classroom had a volume of 123.16 m^3 and was measured using the same method as in the first room. Figure 5 and Figure 6 show the installation of 21 absorber modules in the room from two perspectives. The units were installed at a distance of 10 cm from the ceiling and adjacent walls.

Figure 5. Installation of 21 BATs in classroom, view towards front
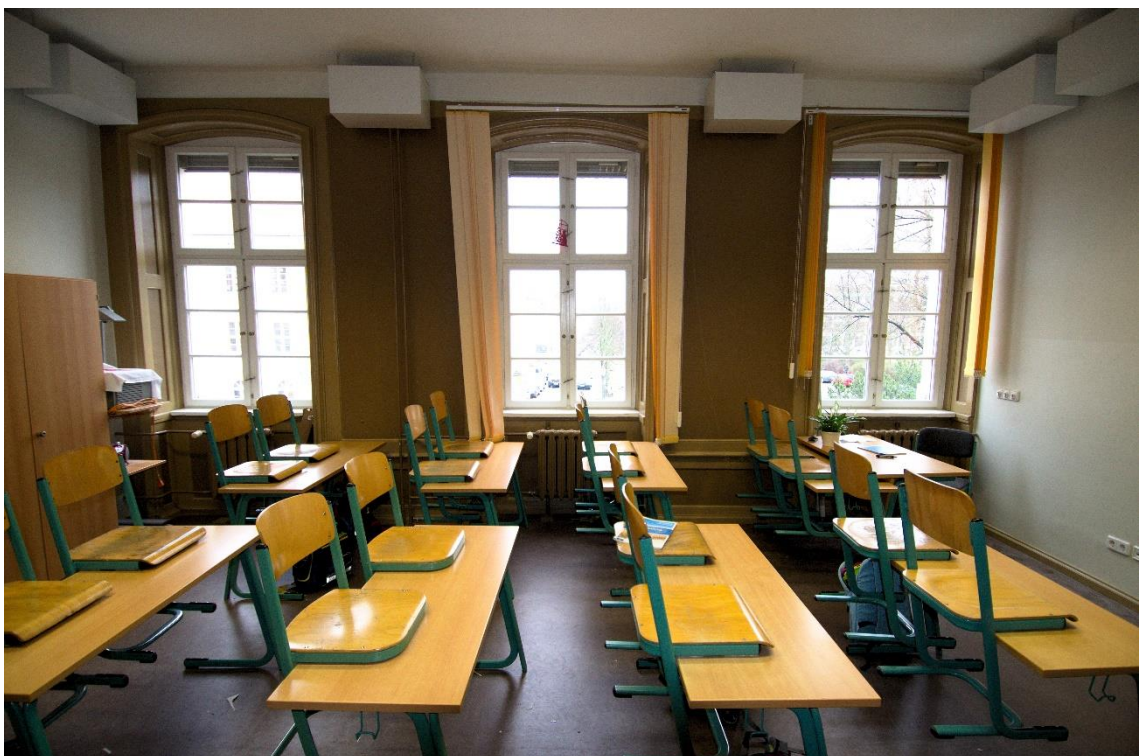
Figure 6. Installation of BATs in classroom, view towards windows

2.4. Impedance tube measurements

A series of impedance tube measurements were taken to examine the surface impedance and absorption coefficients of a BAT probe. The dimensions of available impedance tubes at the TU-Berlin are ø = .1 m, .25 x .25 m, and .5 x .5 m. The dimensions of the BAT are either .3 x .3 m, or .3 x .5 m. As a consequence, a compromise was found by using an especially constructed BAT with the dimensions of .25 x .25 x .25 m. Other than the dimensions, all other characteristics of the unit were identical to the original.

Measurements included placing the BAT at 0, .1, and .2 m from the sound hard end in the tube. In each variation, 2 smooth sides and 2 perforated sides were measured with mineral in 50% and 100% of the inner volume, and an additional variation where the mineral wool was compressed to include 150% fill material. The fill material was the same as the mineral wool used in the BATs in the reverberation chamber tests.

The frequency range of the .25 x .25 m canal is between 20 and 670 Hz, which is the same frequency range of interest for this study.

Traditionally, the surface impedance of a probe measured in an impedance tube has been assessed by creating standing plane waves within the tube with a pure sinus tone frequency generator and speaker at one end, whose frequency range depends on the geometrical parameters of the tube. The probe is placed at the other extremity in front of a sound hard capping, and a microphone is used to find and measure the distance and amplitudes of the first sound pressure maximum and minimum of the incident and reflected waves in front of the probe. These values provide the information needed to calculate the complex reflection factor, from which the surface impedance and absorption coefficients can be derived.

The variables used in the traditional measuring method are related as follows:

the incident plane wave propagating in the x-direction towards the probe:

$$p_i = \hat{p}_0 e^{-jkx} \ [\text{Pa}] \tag{2.4.1}$$

the reflected plane wave returning in the direction of the speaker, where *k* is the complex wave number and $\hat{p}_0$ is the initial wave amplitude

$$p_r = \hat{p}_0 r e^{jkx} \ [\text{Pa}] \tag{2.4.2}$$

25

$$\mu = \frac{\hat{p}_{r,min}}{\hat{p}_{i,max}} \qquad (2.4.3)$$

evaluates the ratio of the amplitude measured at the first minimum of the reflected wave in front of the probe, to the measured amplitude of the first maximum of the incident wave in front of the probe.

$$R = \frac{1 - \mu}{1 + \mu} \qquad (2.4.5)$$

provides the reflection factor, which is the amplitude of the complex reflection coefficient.

$$\varphi = \pi \left(\frac{|x_{min}|}{\frac{\lambda}{4}} \pm 1 \right) \qquad (2.4.6)$$

gives the resulting phase shift in the reflected wave, where x_{min} is the first minimum in the reflected sound wave in front of the probe.

$$r = Re^{j\varphi} \qquad (2.4.7)$$

is the complex reflection coefficient, which is then used to calculate the surface normal impedance

$$\frac{Z_n}{\rho_0 c} = \frac{1 + r}{1 - r}. \qquad (2.4.8)$$

The absorption coefficient is calculated with the reflection factor R, with

$$\alpha = 1 - |R|^2. \qquad (2.4.9)$$

The method described above is extremely time consuming, and for larger probes in impedance tubes with large dimensions, is not a practical method for measuring the necessary reflection coefficients needed for calculating the surface impedance of the probe.

For this reason, the transfer function method was used, utilizing two microphones, whose distance to each other and from the probe are accounted for in the governing equations.

Instead of using single pure tone, a broadband white noise signal is used, and filtered using an FFT and Henning window with 75% overlap. Results were

averaged 100 times during measurement, and the resulting frequency resolution was designated at .625 Hz.

A full description of the measurement procedure may be found in EN – ISO 10534-2.

The impedance is calculated as follows:

Two microphones are placed at positions z_1 and z_2 from the sound hard end of the canal. After measuring once, they are switched to compensate for differences in their respective frequency responses, and the measurement is conducted again.

$$H_{12} = \frac{p(z_2)}{p(z_1)} \qquad (2.4.10)$$

gives the transfer function as a ratio of pressures between microphones 1 and 2, while,

$$H_{12} = \frac{e^{jkz_1} + re^{-jkz_2}}{e^{jkz_1} + re^{-jkz_1}} \qquad (2.4.11)$$

describes more precisely the ratio of the measured pressures, which are both the sum of the incident and reflected soundwaves.

$$r = \frac{H_{12}e^{jkz_1} - e^{jkz_2}}{e^{-jkz_2} - H_{12}e^{-jkz_1}} = Re^{j\varphi} \qquad (2.4.12)$$

again, gives the complex reflection coefficient and reflection factor.

As in the previous method, the normalized impedance Z_n is determined with

$$\frac{Z_n}{\rho_0 c} = \frac{1 + r}{1 - r} \qquad (2.4.13)$$

and finally the absorption coefficients with

$$\alpha = 1 - |R|^2. \qquad (2.4.14)$$

The following figures show the installation of the probe in its various configurations. In each case, both the smooth and perforated sides of the BAT were measured and averaged over two sides of the same type for each.

Figure 7. Installation of BAT in impedance tube at 0 m from sound hard end

Figure 8. Installation of BAT in impedance tube at .1 m from sound hard end

Figure 9. Installation of BAT in impedance tube at .2 m from sound hard end

2.5. Finite Element Method modelling of absorber

The finite element method, or finite element analysis (FEM/FEA), is a numerical procedure for solving partial differential equations in a modelled computational geometric domain. In short, it involves developing a modelling strategy for solving the equations for specific physical phenomena which one would like to observe and analyze, defining the geometric domains, assigning boundary and initial conditions to the model, creating a mesh of the geometrical components, choosing the appropriate solver, running the simulation and interpreting the results. In acoustics, it is useful in modelling or simulating wave propagation and attenuation in gases and solids.

Room acoustical measurements are subject to a larger distribution of steady-state sound pressure measurement and reverberation time results for frequencies corresponding to room modes in small to medium sized spaces, whose modal behavior dominates the sound field at frequencies below the Schroeder frequency. This can create additional challenges for the room acoustical and architectural planning of spaces in which the frequency response in a receiver position is of increased importance. Though the measurements taken in assessing the acoustic quality in spaces in the wave-theoretical frequency range are not necessarily *less accurate,* their general helpfulness significantly declines or adds insecurity to planning measures.

For this reason, it is not only helpful, but sometimes necessary to use wave-theory based modelling methods as opposed to ray-tracing simulations, when the intention of the engineer is to optimize the frequency response for given sender and receiver positions.

Similar to models used in the ray-tracing procedure, FEM models are simplified or idealized representations of the entire domain of observation in which data directly equivalent with or derived from the incident, reflected/scattered, or total soundfield is to be calculated. Small geometric details are generally ignored, as they either increase the calculation time or are acoustically "invisible" for the frequency range in interest. This is not always the case, however, for example when dealing with high-frequency acoustics in which the solid domains have dimensions comparable to the wavelengths present in the study.

Of utmost importance in the FEM process is ultimately the development of the modelling scheme and the most-accurate description of boundary conditions or assumptions for the model, which allow for the more precise computation of the phenomena in question.

In this study, the entire process was broken into multiple modelling procedures in order not only to observe and understand the behavior of the BAT, but to simulate the effect the BAT has on the soundfield in which it is implemented.

2.5.1. Outline of modelling procedure

I. Part one: Solving the surface normal impedance and absorption properties of the BAT module, direct frequency response

1. Schematizing the acoustic problems trying to be solved and developing the proper geometries in order to solve the problem. Proper definition/programming of variables to be calculated utilizing the dependent variables which are solved in the model.

2. Development of a two-dimensional model of the BAT for prototyping and refining of modelling parameters and methods. This was necessary for the faster assessment of simulation results, when attempting to couple the physical interaction between vibrations in the solid domain of the metal plates, the porous domain within the cavity in the BAT, and the air domains in front of and "behind" the BAT.

3. Testing the two-dimensional model with various air cavity sizes, and plate configurations (smooth/perforated, d = 0, 100, and 200 cm).

4. Validating results during mesh refinement and taking advantage of model symmetries. Refining model to decrease computational time without affecting results.

5. Conversion of the two-dimensional models into three dimensions.

6. Debugging the model, which is now subject to more complex modelling restraints and definitions.

7. Again, refining boundary parameters influencing the acoustic-structure interaction, as well as observing the influence of sampling or integration points and surfaces at which the computed variables are evaluated.

8. Post-processing results and comparison with previous measurements

II. Part two: Implementation of calculations from part one into room model; a direct frequency response computation

1. Developing a second modelling scheme for solving the modal damping problem necessary for observing the effect the BAT modules have on the direct frequency response at receiver positions in the designated sound field. No programming necessary of variables solved in this model, since the desired sound pressure is automatically evaluated.

2. Geometric modelling of space and definition of sender and receiver positions.

3. Prototyping model strategy to debug modelling errors.

4. Increasing geometric complexity of domains until the correct relationship between absorber surface placement and air domains could be found monitoring computational costs. Results observed for plausibility, by comparing initial calculations of room model with and without damping.

5. Development of a set of absorber placement permutations.

6. The number of model computations increases as result of step 5, which makes the testing of iterative solvers necessary for decreasing calculation time.

7. Solving all model permutations.

8. Exporting results and post-processing in MATLAB.

9. Analysis of results.

2.5.2. Theory of FEM for acoustics

A full mathematical derivation of the theory behind the finite element method may vary depending on the literature, though the general principles are the same. Additionally, the modelling software used may use differing methods for converting and solving the governing equations. Various commercial FEM software packages exist for solving partial differential equations in acoustics, the most popular being ACTRAN, Abaqus, and COMSOL. COMSOL Multiphysics was used for this study.

The basic theory presented here is given in full in section 3.5 of *Room Acoustics* (Kuttruff, 2017). Details regarding test functions may be found in chapter 10 of *Computational Acoustics* (Bergman, 2018).

The numerical procedure of the finite element method involves the conversion of the modified Helmholtz equation into a system of linear equations, which is then solved by either a direct or iterative solver.

The first equation is the modified Helmholtz equation,

$$\iiint_V [\Delta p + k^2 p + i\omega\rho_0 q(r)]v(r)dV = 0 \tag{2.5.1}$$

where

V is the domain in which the equation is to be solved,

$v(r)$ is the set of test, or basis functions used to approximate the behavior of the dependent variable in the interior of an element. They tend to be known, well behaved continuous functions.

An element is a discretized section of a larger domain, containing anywhere from 2 to 20 nodes, or points which make up the mesh created by the geometry. Element size depends on the frequency range of interest in the study. Generally, the maximum element size may be given by $\frac{\lambda_{min}}{6}$, with λ_{min} being the highest frequency in the study. Additionally,

$q(r)$ represents the source density function at point r in the domain V.

The Helmholtz equation is converted to

$$(\mathbf{K} - k^2\mathbf{M} + ik\mathbf{C}) \cdot \mathbf{p} = ik\rho_0 c\mathbf{Q} \qquad (2.5.2)$$

where $\mathbf{K}$, $\mathbf{M}$, and $\mathbf{C}$ represent the following matrices:

$$K_{mn} = \iiint_V \nabla\Lambda_m \cdot \nabla\Lambda_n dV \qquad (2.5.3)$$

is the stiffness matrix, or the system of linear equations to be solved, while

Λ_m and Λ_n are the shape functions used for approximating the solution in an element. When both indices are the same, the function equals 1, it is otherwise 0;

$$M_{mn} = \iiint_V \Lambda_m\Lambda_n dV \qquad (2.5.4)$$

Is the mass matrix, the elements of which are defined by the product of the base functions within the given domain,

$$C_{mn} = \iint_S \Lambda_m\Lambda_n \frac{dS}{\varsigma} \qquad (2.5.5)$$

is the damping matrix, which models the interpolating functions at the boundaries of the volume. These matrices are multiplied with

$\mathbf{p}$; the set of coefficients providing the amplitudes (complex pressure amplitude) of the shape functions, and finally $\mathbf{Q}$ may be understood as a source within the volume with

$$Q_m = \iiint_V q\Lambda_m dV . \qquad (2.5.6)$$

2.5.3. Development of a model for simulating surface impedance of BAT module, two-dimensional

As previously described, after deliberating and testing a series modelling schemes, it was found to be most advantageous to first simplify the problem and break it down into steps. A basic form of the impedance problem is the 2-dimensional representation of the domains with appropriate material properties as a series of layers through which a plane wave propagates, as described in Figures 10-13.

Figure 10. Overview of FEM model geometry, domains, and dimensions
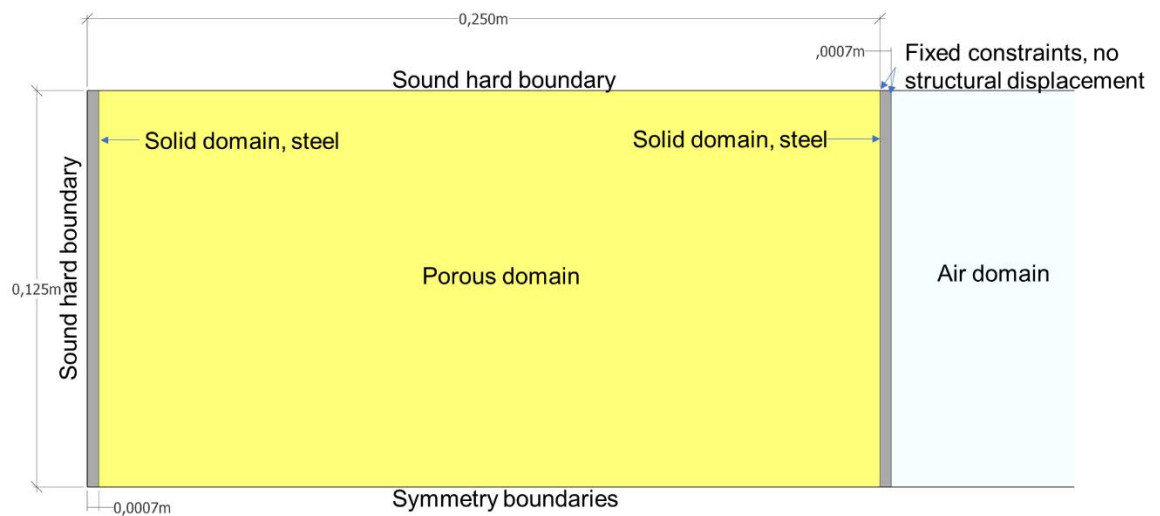
Figure 11. Detail of model domains including boundary conditions
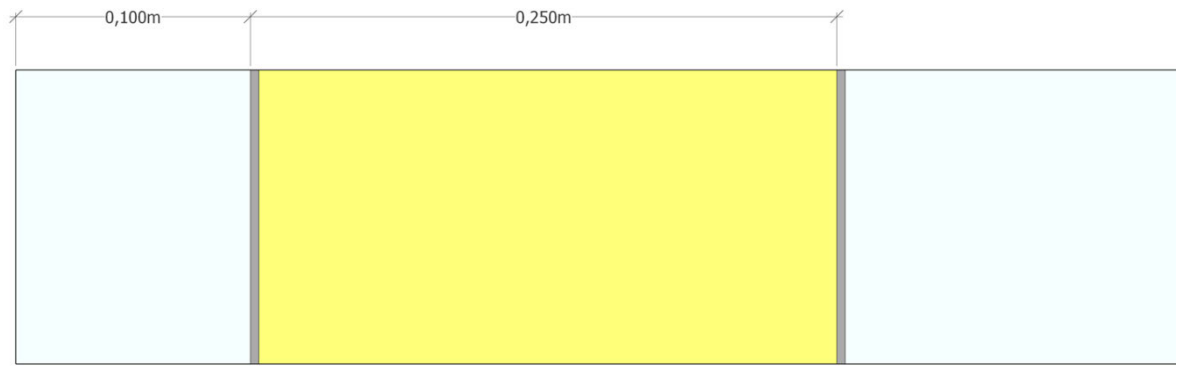
Figure 12. 2D FEM model with 10 cm air cavity
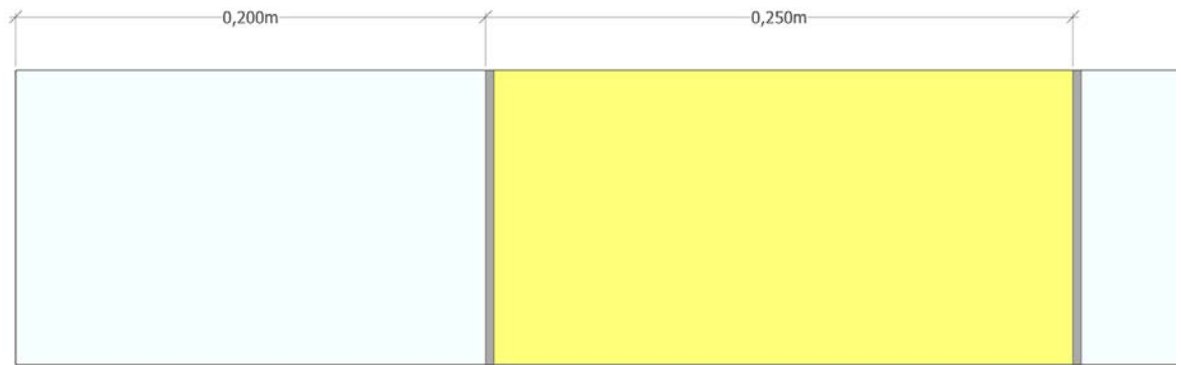
Figure 13. 2D FEM model with 20 cm air cavity

The model was designed to account for the pressure field caused by the impinging plane wave on the BAT surface, as well as the structural displacement caused by the plate resonances of the metal (solid) domains. For this reason, it was not physically correct or possible to sample or integrate directly *on* the surface of the front plate in the model, rather 1 mm in front of it as shown in Figure 14, when calculating the reflection factor. Given the frequency range in question however, this did not affect the results when calculating the absorption coefficient. Additionally, the integrating distance was tested at various distances from the BAT, and there was no noticeable effect in any of the distances tested.
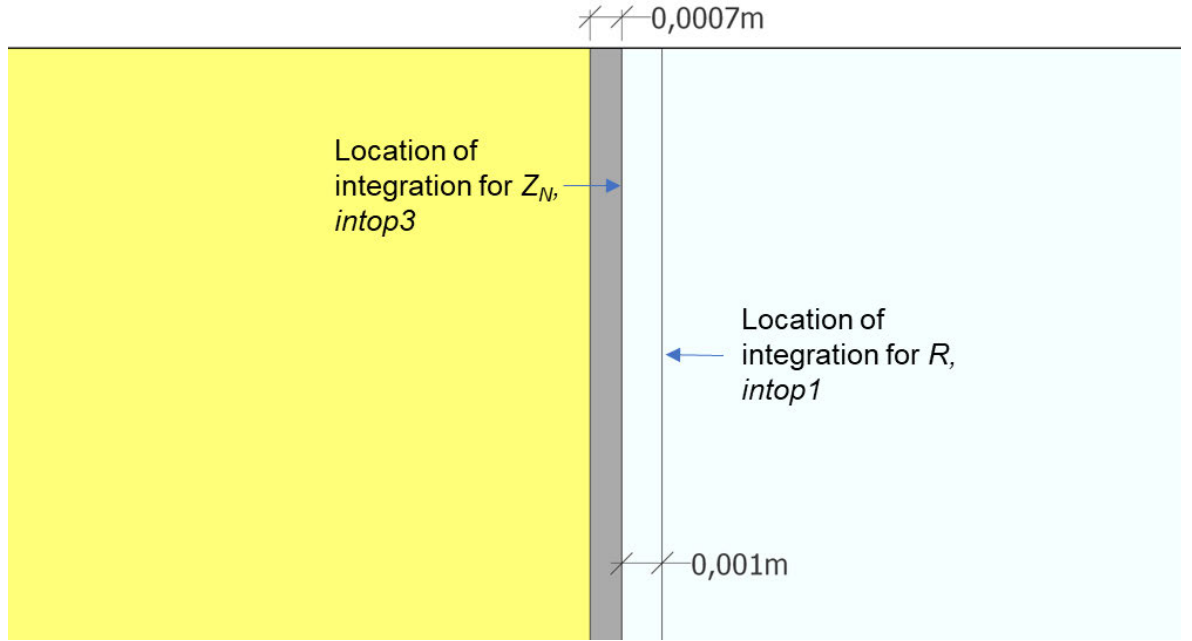
Figure 14. Locations of integration lines for impedance and reflection factor calculations

The surface impedance was programmed and calculated with the following formula:

$$Z_N = \frac{1}{c_0 \rho_0} \left(\frac{intop3(acpr.p_t)}{intop3(-acpr.vz)} \right) \tag{2.5.7}$$

Where *intop3* is the integration operator, whose location is shown above in figure 13.

acpr.p_t defines the total sound pressure field,

-acpr.vz is the velocity in orthogonal to the plate surface,

c_0 is the speed of sound, 343 m/s, and

ρ_0 is the density of the air in front of the plate, defined as 1.12 kg/m^3.

The reflection factor was calculated with:

$$R = \frac{intop1\big(down(p_{scat})\big)}{intop1\big(down(p_{inc})\big)} \tag{2.5.8}$$

where

intop1 is the integration operator shown in figure 13,

37

p_scat is the pressure of the scattered sound field at the location of *intop1,* and *p_inc*, is the pressure of the incident sound wave also at the location *intop1*. Both values are real and give the amplitude of the calculated pressure.

The incident soundwave was defined as a plane wave travelling in the negative z-direction, orthogonal to the surface of the plates, which is seen in Figure 15. The wave is defined as a *background pressure field*, given by the following formula:

$$p_b = p_0 e^{i\phi} e^{-ik_s \frac{(x \cdot e_k)}{|e_k|}} [\text{Pa}]$$ (2.5.9)

where

p_0 is the amplitude of the plane wave, set to 1 Pa,

ϕ is the phase of the wave, set to 0 radians, and

$$k_s = \frac{\omega^2}{c^2}$$ (2.5.10)

gives the wave vector, orientated with displacement x and elementary vectors

e_k, where *x = 0, y = 0*, and *z = -1*.
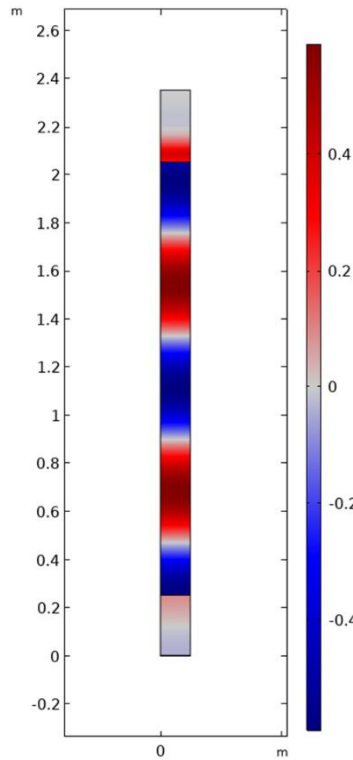
Figure 15. Incident plane wave normal to absorber surface in 2D FEM model

The meshes for the initial models, shown in Figure 16, were created with two different types of elements. At the top of the model, 2-dimensional rectangular, or "mapped", elements were used, since this layer was created to "release" or allow the complete further propagation of reflected plane waves outside of the model. The elements in the subsequent layers consisted of free triangular elements, which have the advantage of being able to smoothly adapt to smaller element sizes when layer thicknesses rapidly change, as they do when transitioning from the air domain to the solid domain.

As previously mentioned, the maximum element size is given by $\frac{\lambda_{min}}{6}$, with λ_{min} being the highest frequency in the study. The minimum element size is dictated by the smallest or most narrow region in the domains, in this case, the .7 mm plate, the solid domain.
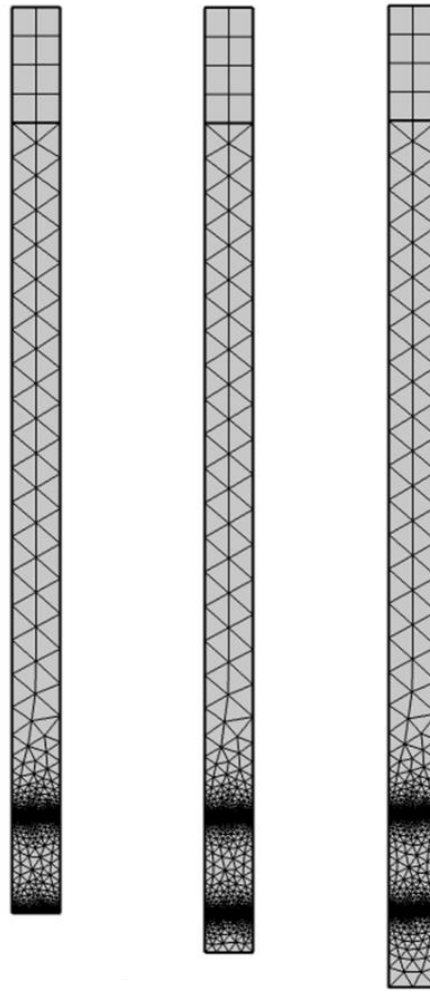
Figure 16. Meshes of 2D FEM model with a 0 (left), 10 cm (middle), and 20 cm (right) air cavity below absorber

39

The porous domain, defined as the interior domain of the BAT, is characterized by a porous material with a flow resistance using the simplest model, Delany-Bazley (1970), given the lack of additional information about the material. The flow resistance of the elastic material is given as 5000 Pa*s/m^2, whose fluid properties are those of air.

The solid domain is defined as steel, requiring more material parameter definitions including the density, Young's modulus, Poisson's ratio, and speed of sound in steel. The mentioned parameters are defined with:

$\rho_{steel} = 7850 \frac{\text{kg}}{\text{m}^3}$; density of steel

$E = 205 \times 10^9$ Pa; Young's Modulus

$v = 0.28$; Poisson's ratio, and

$c_{steel} = 5800 \frac{\text{m}}{\text{s}}$; speed of sound in steel.

Finally, one long side of the model was defined with a symmetry boundary condition, while all the others were defined as sound hard as shown in Figure 17. The symmetry decreases the number of elements, edges, and nodes by one half, significantly decreasing the computational cost and time. Points connecting the steel plate to the sound hard edge were defined with a fixed constraint boundary condition.
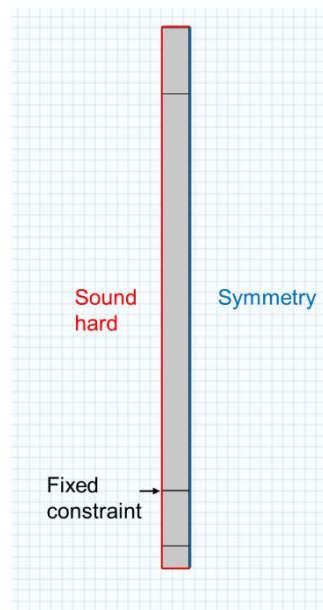
Figure 17. Exterior boundary conditions of 2D FEM model

Conveniently, COMSOL Multiphysics contains a native interior perforated plate boundary condition, for which the user may define geometrical parameters as well as fluid properties. The boundary described in the model containing the perforated plate contained the following parameter values:

$d_h = 0.0075$ m; diameter of the perforation holes,

$t_p = 0.007$ m; plate thickness,

$\sigma = 0.22$; area porosity

The properties of the surrounding fluid are those of air, including the density ρ_0, speed of sound c_0, and the dynamic viscosity μ. End correction and hole-hole interaction are automatically accounted for.

Finally, the model was solved for the frequency range 20 – 630 Hz, with a 1/6th octave resolution. The stationary solver used in this model was MUMPS, a standard, highly robust FEM solver able to solve very large matrices containing both real and complex values. The computation time for this simplified model generally did not exceed 4 minutes, which allowed for fast prototyping and a quick analysis of results for refining the model.

2.5.4. Development of a model for simulating specific impedance of BAT module, three-dimensional

After testing and validating the initial simplified model, the same strategy was used for developing the 3-dimensional model. All of the geometrical and material parameters remained constant. The only major challenge in transitioning to three dimensions was the coupling of the pressure acoustic and structural acoustic interactions while defining the domains. Here, it was necessary to allow the software to calculate the pressure acoustics for all domains, while calculating only the solid domains in the structural acoustic node. This was not the case in the two-dimensional model, which required less material property information.

Again, separate models were developed for simulating the modules with 0 cm air cavities, as well as the smooth and perforated sides. After validating the 25 cm model, a 30 cm model was created for the final computations, which more precisely simulates the actual BAT.

A major difference between the two models was the number of elements which had to be calculated. The three-dimensional models contained two orders of magnitude more elements than the two-dimensional models.

This necessitated the usage of an iterative solver, as opposed to the direct solver used previously. Iterative solvers are helpful when solving more complex, larger models, as they tend to use less memory and provide faster results. The accuracy of results has to be observed though through comparison with a model computed with a direct solver. In this case, the solver used was GMRES solver, or generalized minimal residual solver, with a maximum of 10,000 iterations.

Shown below in Figure 18 is the general modelling strategy, which very closely resembles the testing method and physical characteristics of an impedance tube.
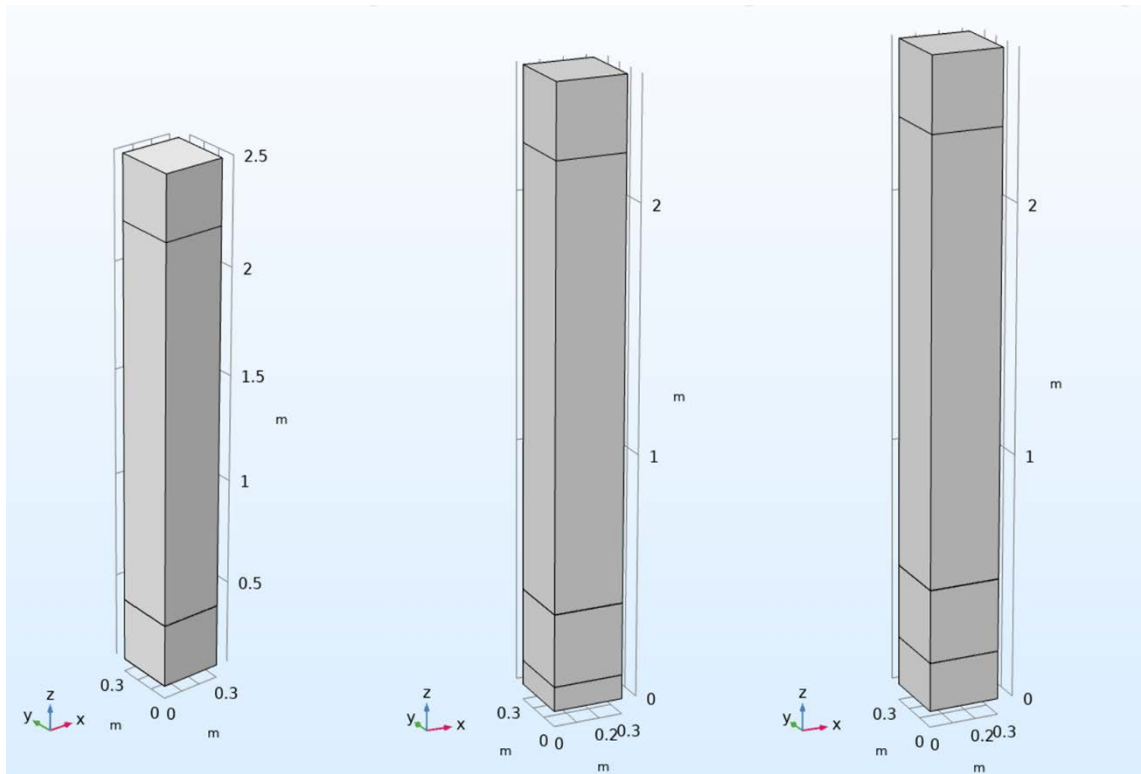
Figure 18. Impedance tube-like modelling strategy used in the 3D FEM model for 0 cm (left), 10 cm (middle), and 20 cm (right) models

Additionally, in Figure 19 one can clearly see the significant increase in meshing elements, caused by the addition of a third dimension. For the three-dimensional model, the meshing parameters remained the same as in the two-dimensional models. No boundary conditions were changed, though each condition type included a greater number of boundaries or edges to include.
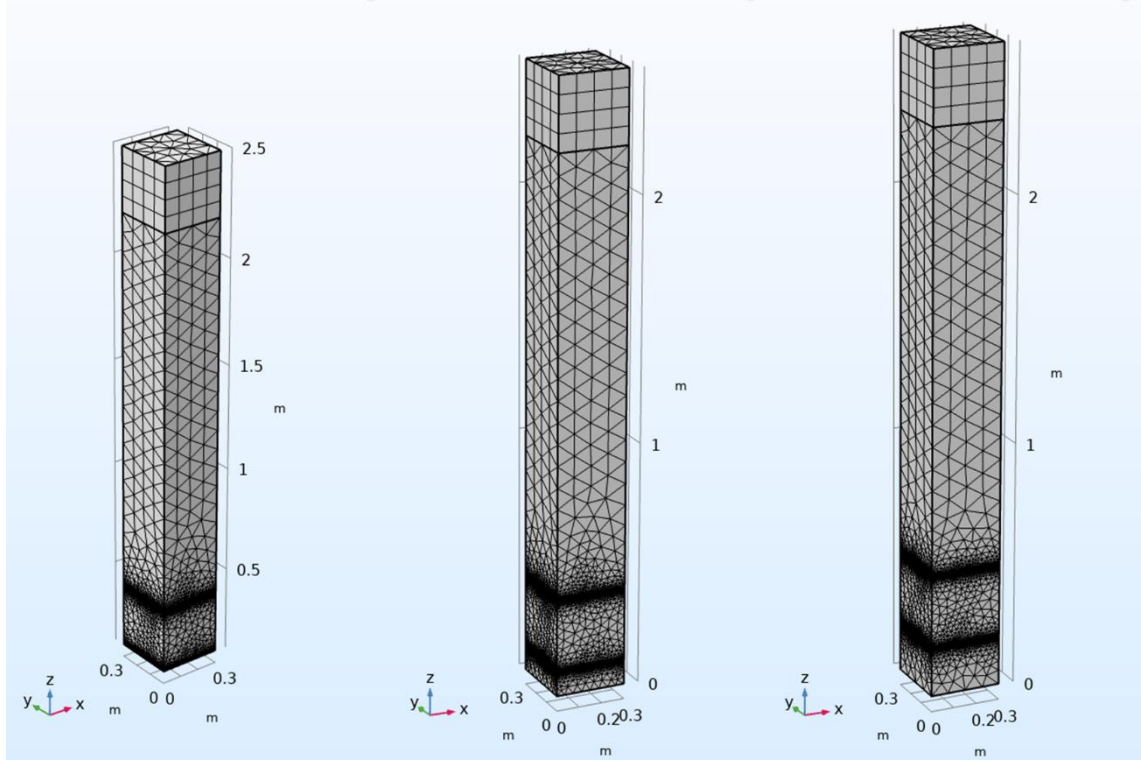
Figure 19. Meshes of 3D FEM models

The propagation of plane waves with differing wavelengths are visible after solving the model (see Figure 20). In a real impedance tube, one would encounter the development of cross-sectional modes at higher frequencies (not shown here) above the tube cutoff frequency, however this is not the case when using an FEM model which allows for the definition of a background pressure field.

43
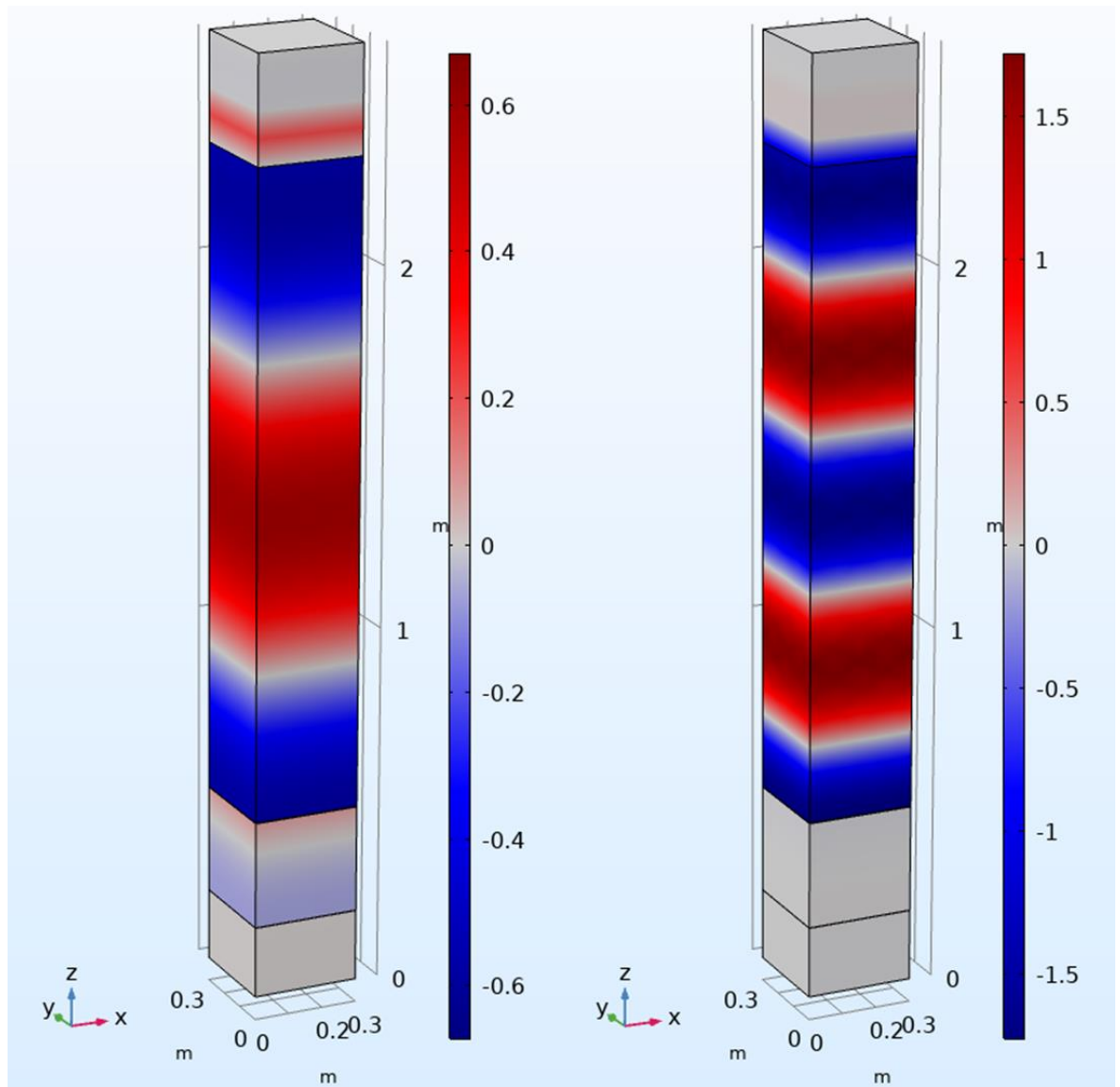
Figure 20. Plane waves of different wavelengths propagating in 3D FEM model

2.6. FEM simulation of modal damping in a room with absorber modules

The BATs were designed in part to attenuate low frequency room modes. The extent to which they achieve exactly that objective can be shown by simulating the BATs in a virtual room environment. Since the ray tracing method cannot model sound pressure field resulting from discrete room mode shapes, the procedure must again be conducted using the finite element method.

The procedure described here relies heavily on the results from the previous simulation. The model, however, utilizes the same principles, though with different geometries, boundary conditions, source type, and sampling strategies.

Finally, the results of the model are used to show the effect the BAT has on the direct frequency response at discrete positions within the sound field.

This section describes the modelling strategy and process, followed by the results and analysis.

2.6.1. Development of a room model implementing the BAT modules

In order to observe the effect the BATs have on the sound field within a virtual space, it is necessary to simulate the room in two states using separate models, namely an undamped and damped state, then observe the difference.

The basic components of the undamped room model involve the room geometry, a point source, and an array of observation positions, or virtual "microphones".

The damped room model however includes the simplified geometry of rows of BAT modules in various permutations of their positioning and as a result number. The surface of the BAT is defined with a wall impedance boundary condition, whose values are taken from the results of the BAT surface normal impedance simulation.

Since the modules are free floating cavities within the larger space, it is not possible to compare them with the analytic analogue of a rectangular room with non-rigid boundaries, for which an exact solution exists. The necessity to use a numerical method is justified by the complex geometry created by inserting a non-

45

rigid boundary into the space, whose outer boundaries are defined as uniformly rigid.

2.6.2. The undamped room model

The undamped room model was created within the COMSOL CAD modelling interface. Since the dimensions of the room are somewhat arbitrary, the room was simply defined as a 3 x 5 x 3 m volume, as shown in Figure 21, and the partitioning of the domains are visible on the boundaries of the model. All external boundaries in this model and the damped model have been defined as rigid, or sound hard.
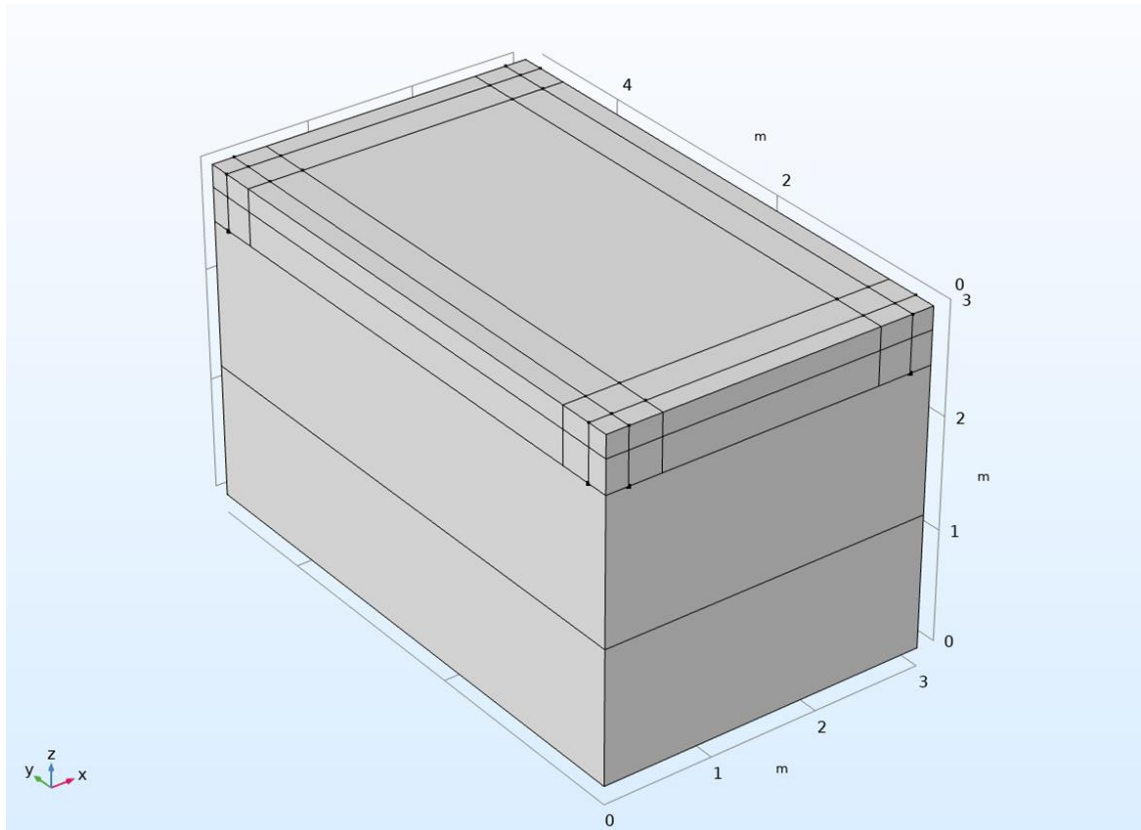
Figure 21. Geometry of undamped room model with domains visible on outer surfaces

The transparent (Figure 22) and wireframe (Figure 23) renderings show more clearly how the interior of the model is broken into multiple domains. The point source, not shown here, is located at the point (1.5, 0, 1.2) from the origin at the lower left, and has a volume flow rate of 10^{-5} m³/s.
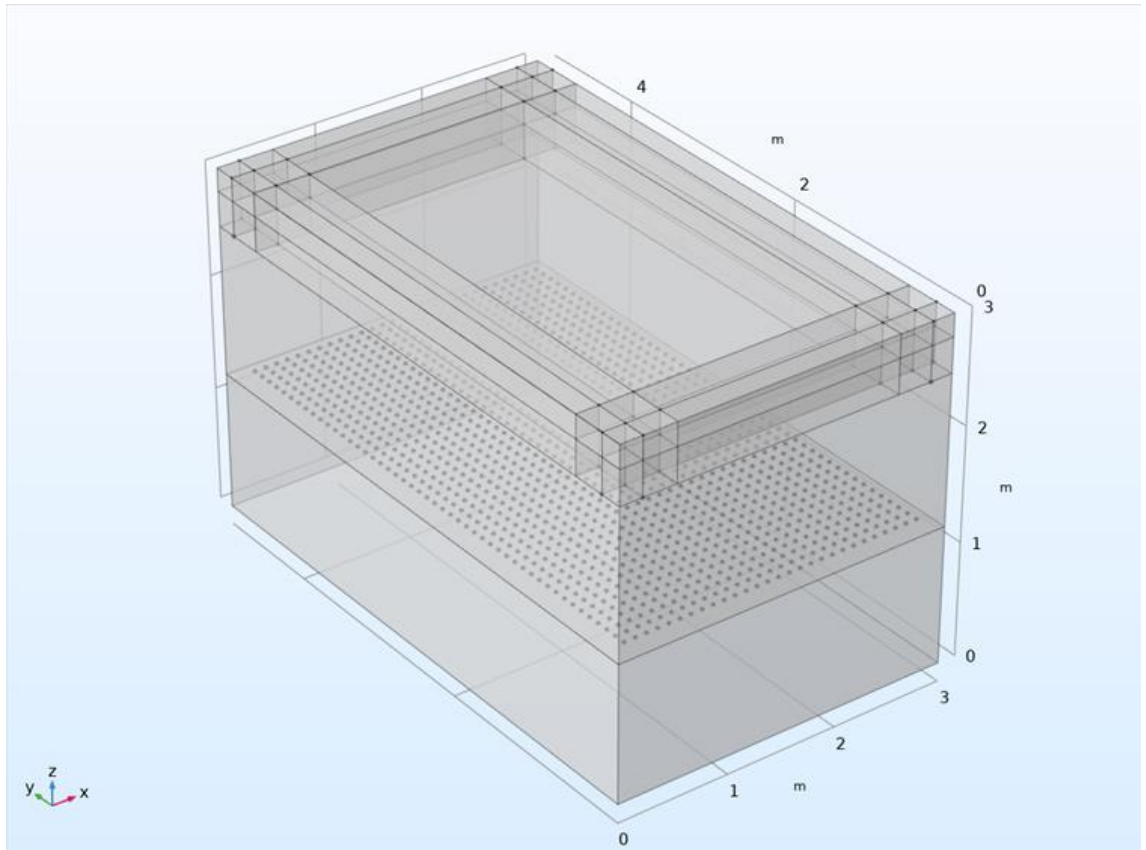
Figure 22. Transparent rendering of undamped room model
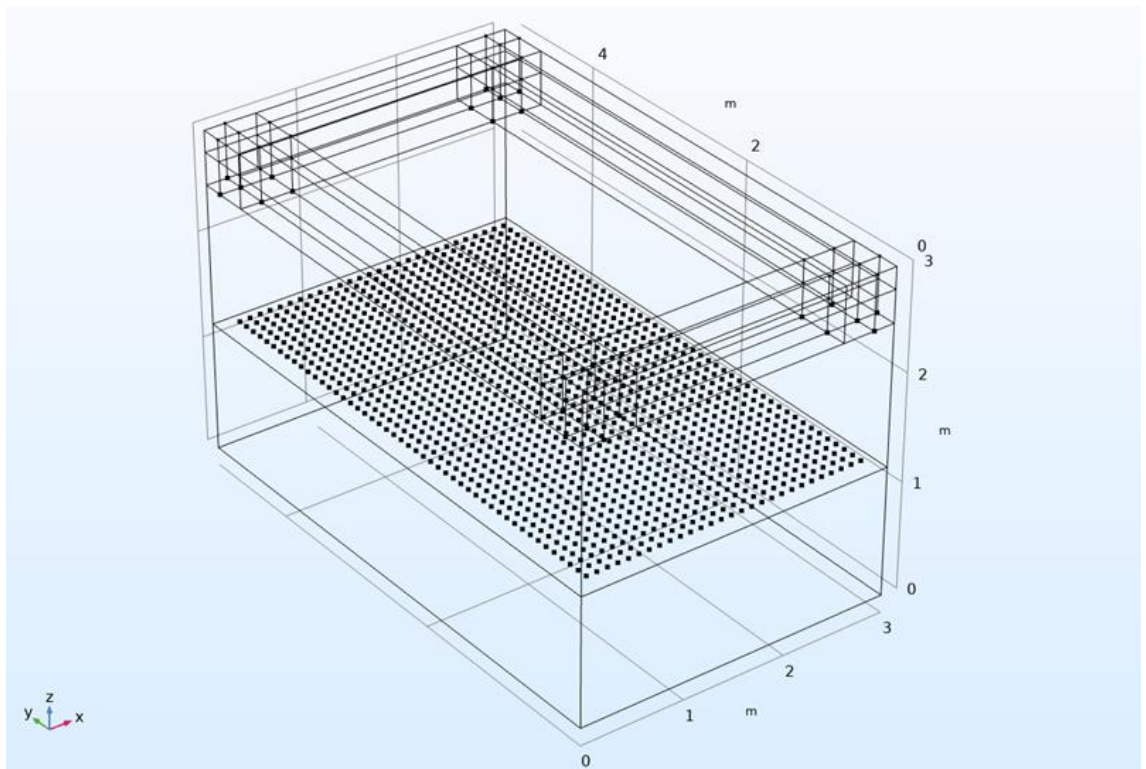
Figure 23. Wireframe rendering of undamped room model

In the undamped version of the model, all the surfaces created by the partitioning of the upper domain of the model were defined as sound soft, so that sound waves pass through unhindered. At a height of z = 1.2 m, an array of 28 x 48 points was created for sampling the resulting simulated frequency response in the frequency range of 20 to 630 Hz. This model was solved using the standard direct MUMPS solver, which calculated the pressure field within the entire domain, with a load given by the point source.

Similarly to the BAT model, the room model consists of a mesh consisting solely of tetrahedral elements as seen in Figure 24, allowing for the smooth size transition between larger and smaller domains. The density of the mesh increases significantly at the central horizontal partition to allow for a finer resolution at and around the frequency response sampling points.
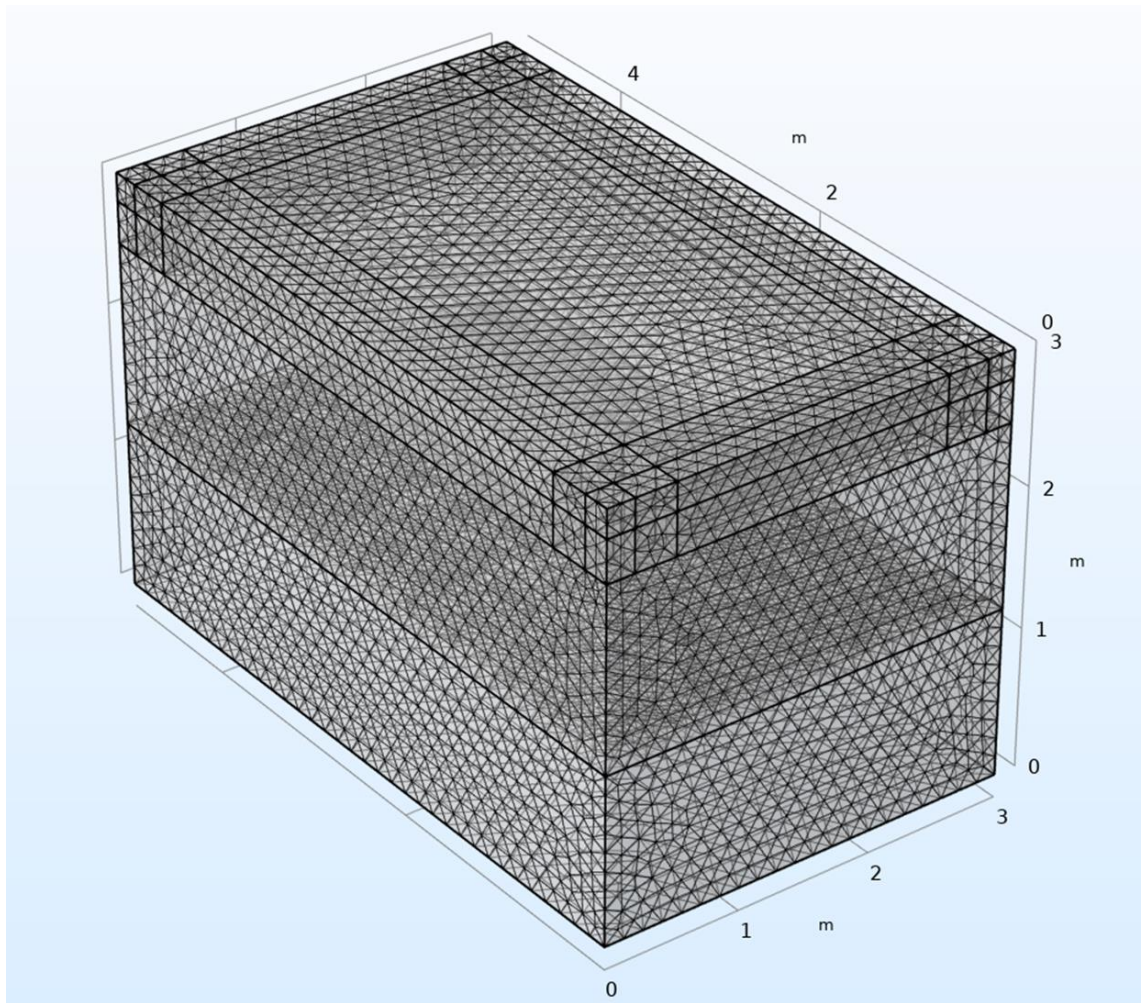
Figure 24. Mesh of undamped room model

2.6.3. The damped room models

The geometry of the damped room model is generally the same as the undamped room model, however it also contains an additional set of domains within the main cavity, the surfaces of which were used for defining the non-rigid boundaries. Figure 25-28 show the geometry and domains.
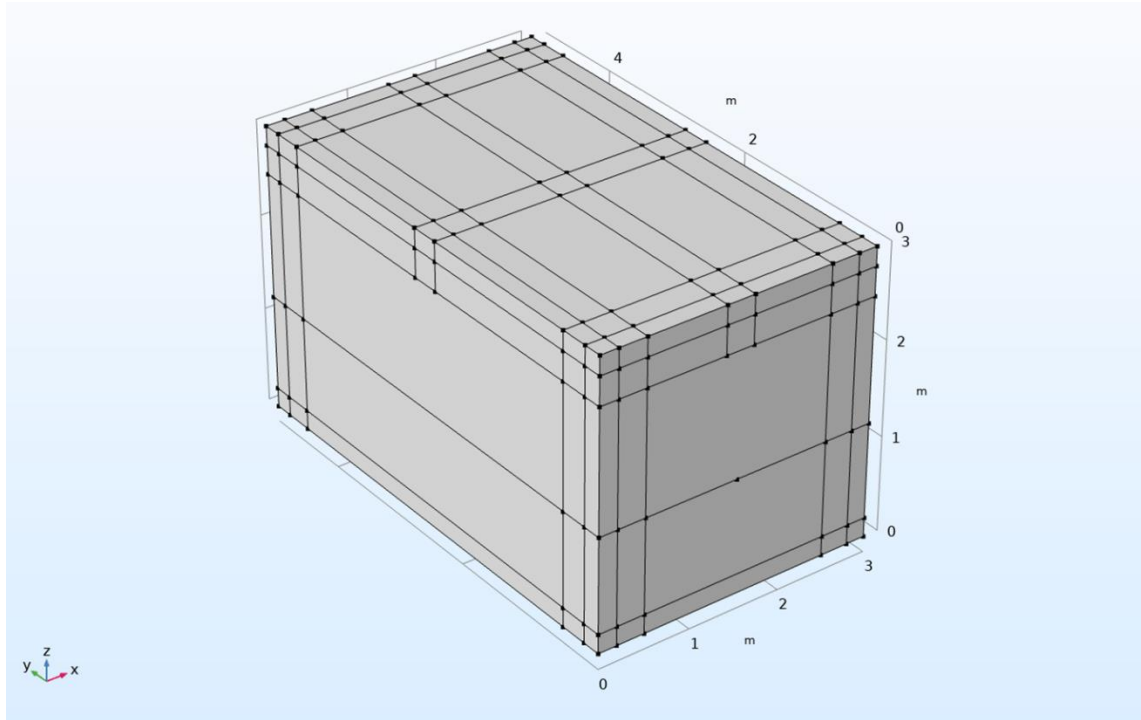
Figure 25. Geometry of damped room model
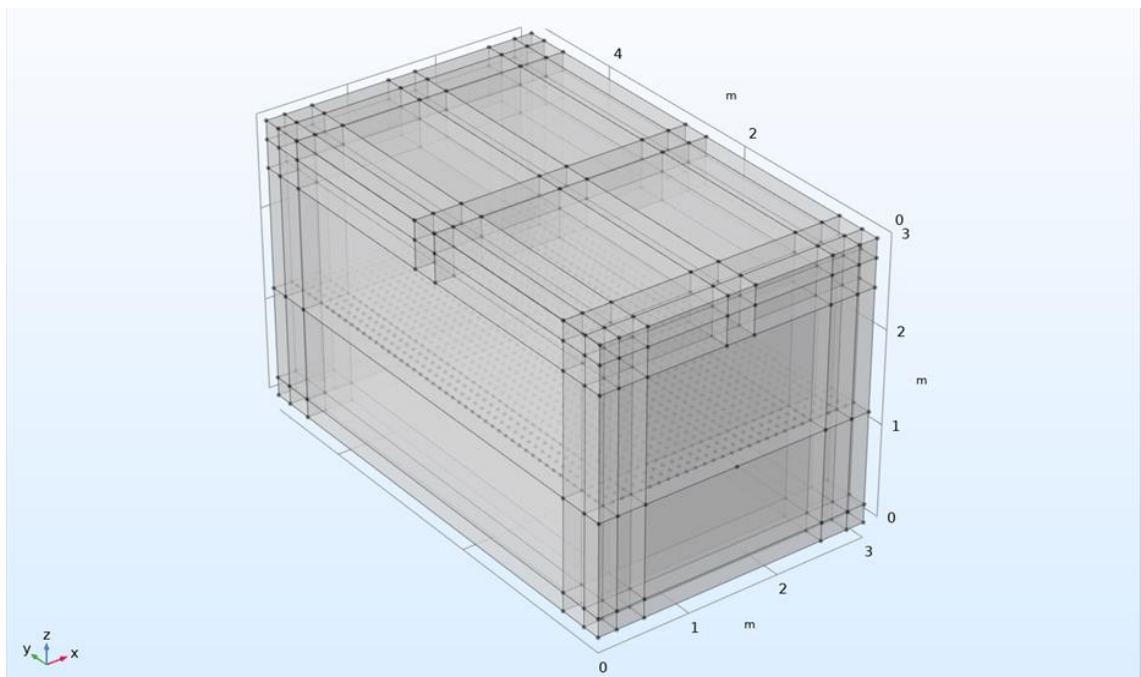
Figure 26. Transparent rendering of damped room model

49
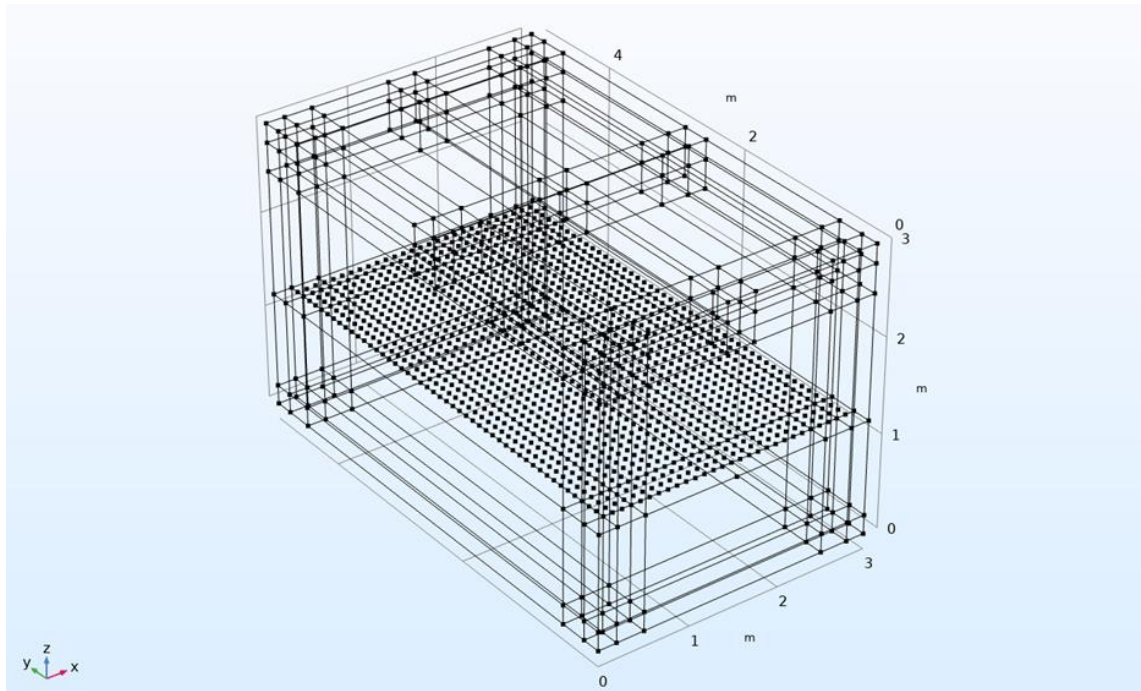
Figure 27. Wireframe rendering of damped room model
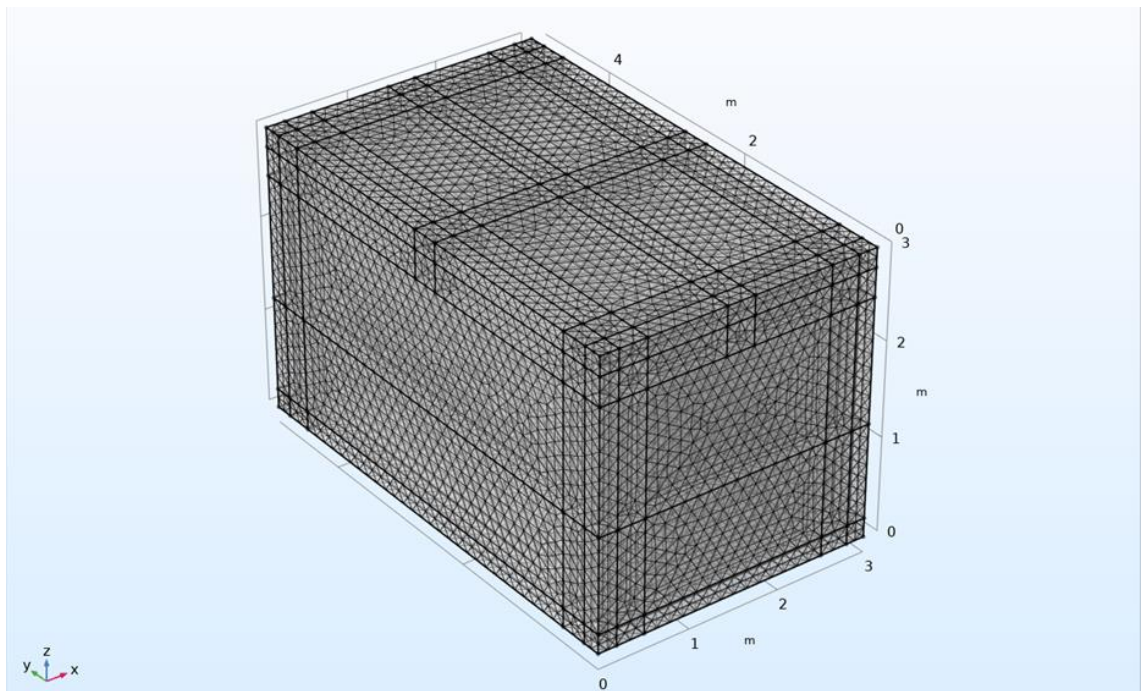
Figure 28. Mesh of damped room model

The above renderings show the increased complexity of the inner geometry as well as the mesh. A total of 20 permutations of absorber positioning configurations were simulated. For each permutation, the domains designated as absorbers were defined as being external to the model, so that the surfaces adjacent to the interior of the room were considered external boundaries; an important definition, which allowed the surfaces to be assigned the impedance boundary condition.

One of the other most important steps in the modelling procedure was defining the impedance boundary conditions of the BAT modules, the values for which were derived from the BAT module studies. The definition required the creation of four interpolation functions, each assigned to a specific part of the impedance for the smooth and perforated surfaces. The definitions were separated into the real part of the smooth surface at d = 20 cm, the imaginary part of the smooth surface at d = 20 cm, the real part of the perforated surface at d = 20 cm, and the imaginary part of the perforated surface impedance at d = 20 cm. The impedance boundary condition itself took on the form:

$$Z_{surface}(f) = real_{surface}(f) + i \cdot imag_{surface}(f). \qquad (2.6.1)$$

In total, 21 models were used for the analysis. This includes the 20 permutations of the damped model, and 1 undamped model. In each of the damped models, two long faces of each absorber row were defined with the perforated plate impedance boundary condition, while the other two long faces and two end faces were defined with the smooth plate impedance boundary condition. The absorber configurations can be seen in Figure 29.
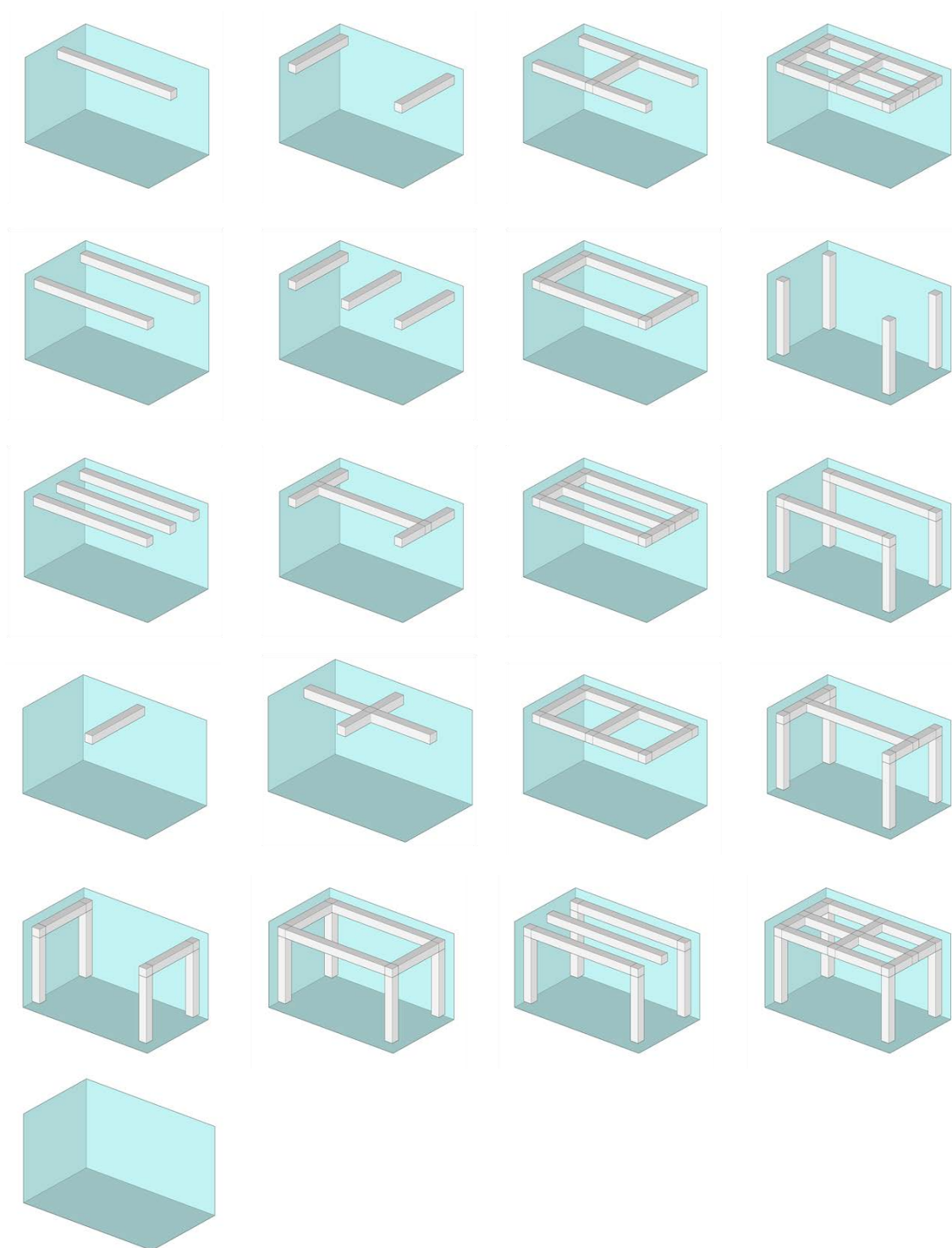
Figure 29. Permutations of absorber module configurations used in damped and undamped room models

3. Results

In the following sections the results of the individual measurements and simulations will be presented followed by an analysis of the results and correlations between the data.

3.1. Reverberation chamber measurements

A calculation of the aequivalent absorption area using equation 2.2.1. from the measurement of 12 BAT modules is shown here in Figure 30. The results, which show a significant increase in A_{eq} between 80 and 315 Hz, and flattening out above 400 Hz, were then converted to absorption coefficients using equation 2.2.3., as shown in Figure 31, using the individual the surface area values introduced in Figure 2.
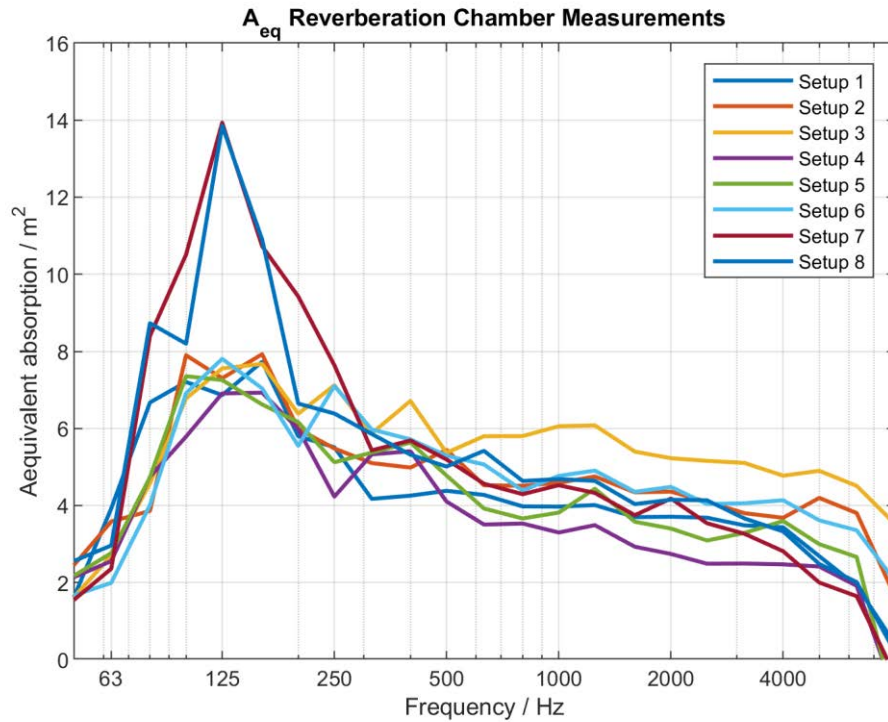
Figure 30. Aequivalent absorption area of 12 BATs measured in a reverberation chamber in various configurations

Again, the absorption coefficients peak at a value of 1.28 at 125 Hz, and tapers steeply towards lower frequencies though more slowly approaching 4000 Hz. Absorption coefficients above 1 are generally a result of measuring objects of

larger volumes which leads to an edge diffraction effect, which is not an uncommon phenomenon in reverberation chamber measurements.
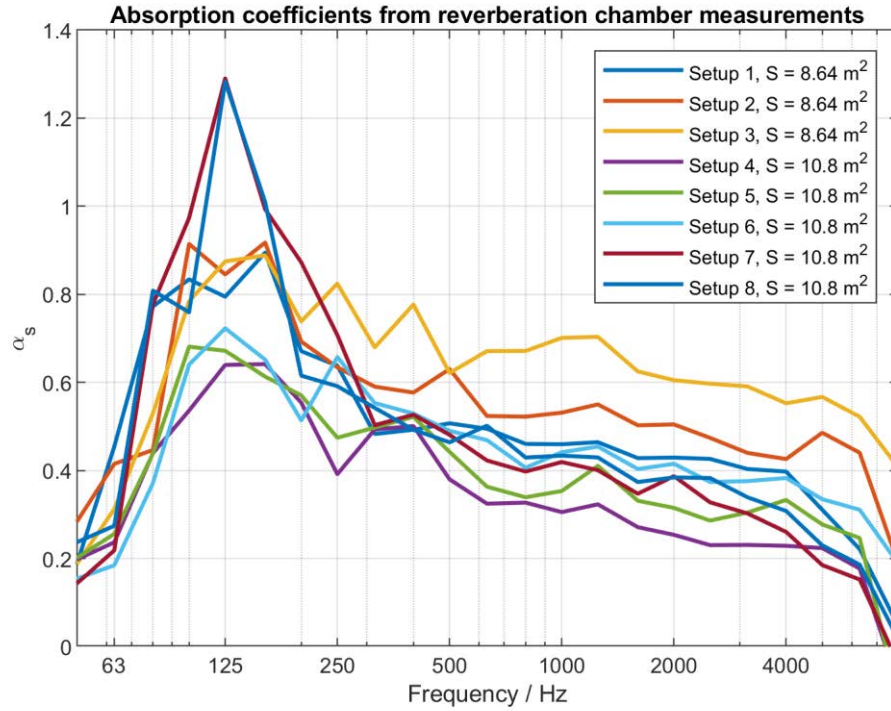
Figure 31. Absorption coefficients of BATs measured in reverberation chamber

Finally, the arithmetic mean shown in Figure 32 of the absorption coefficients was calculated with equation 2.2.3., resulting in a set of coefficients reflecting the above results. Here, we see again a maximum at 125 Hz with a value of 0.89, providing a more physically useful reference for calculating expected reverberation times when implementing the BAT in actual rooms, as will be shown in the next set of results.
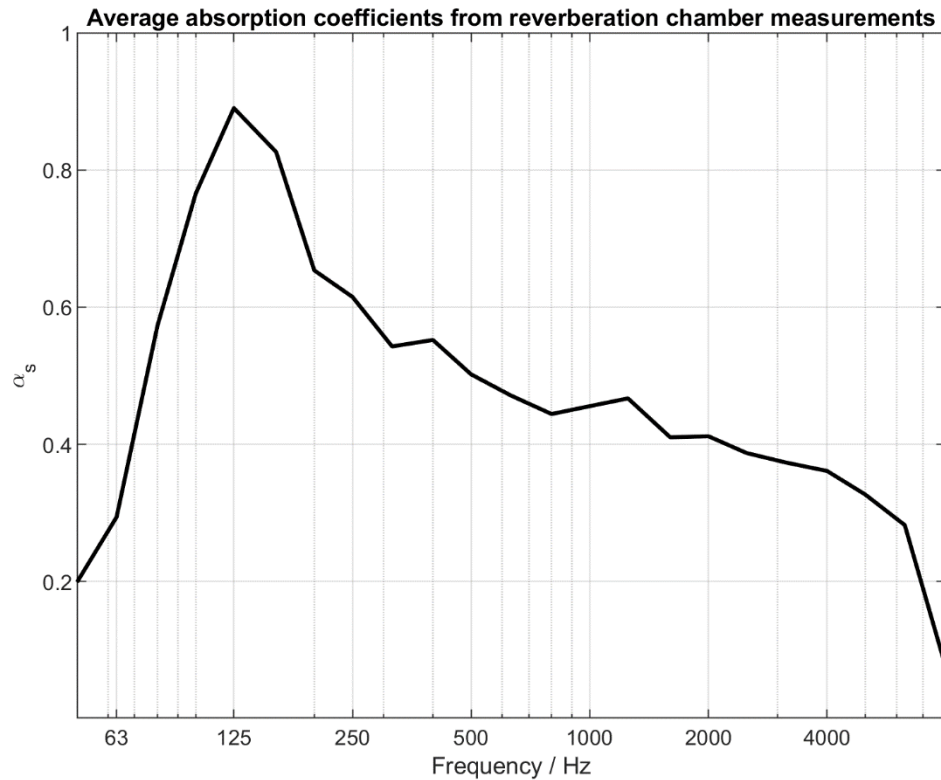
Figure 32. Arithmetic mean of absorption coefficients obtained from reverberation chamber measurements

3.2. Measured reverberation times in sample rooms

As discussed in section 2.3., the BATs were implemented in two sample rooms. The first room was a small meeting room in a facility where scientific instruments are developed, whose volume was 73 m^3. The reverberation times were measured before and after the implementation of 15 BAT modules. The results in Figure 33 show a broadband reduction in the reverberation time around and below 250 Hz, with a maximum reduction at 250 and 100 Hz of .6 seconds, while more modest reductions between .22 and .35 seconds are seen above 500 Hz.

A similar tendency may be found in the results shown in Figure 34 of the reverberation time measurements taken in a 123.1 m^3 classroom, though a maximum reduction of 0.54 seconds is found this time at 160 Hz extending up to 250 Hz. The difference in reverberation times between the *before* and *after* states below 125 Hz and above 250 Hz decrease, as to be expected given the absorption coefficients calculated from the reverberation chamber measurements.
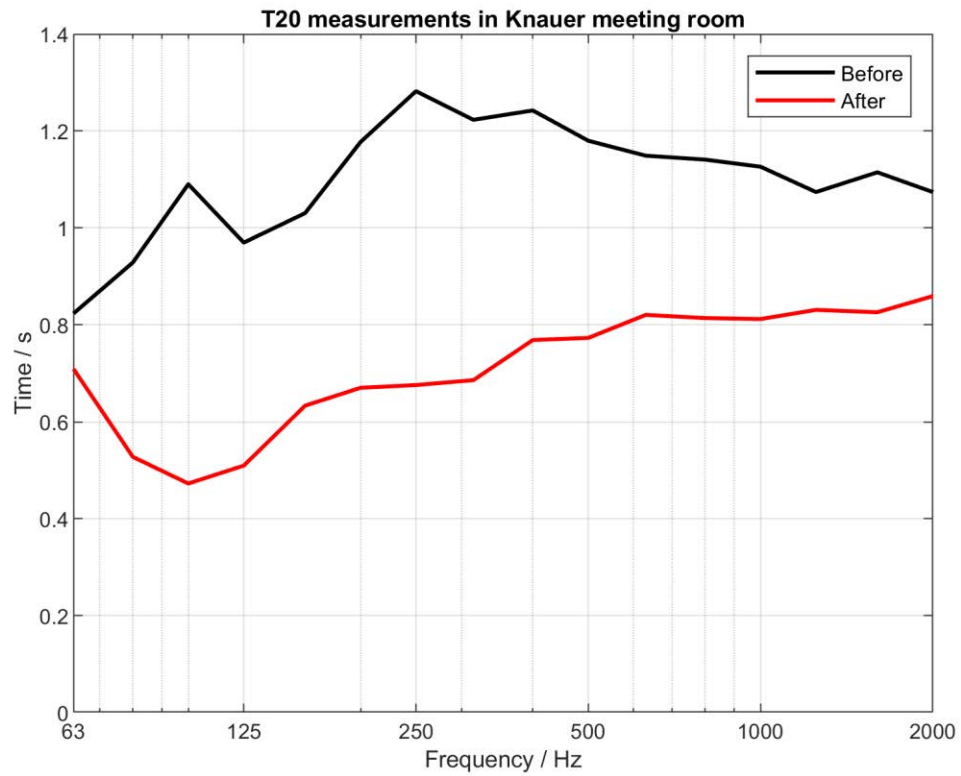
Figure 33. Measured reverberation times of a 73 m³ meeting room treated with 15 BAT modules before and after installation
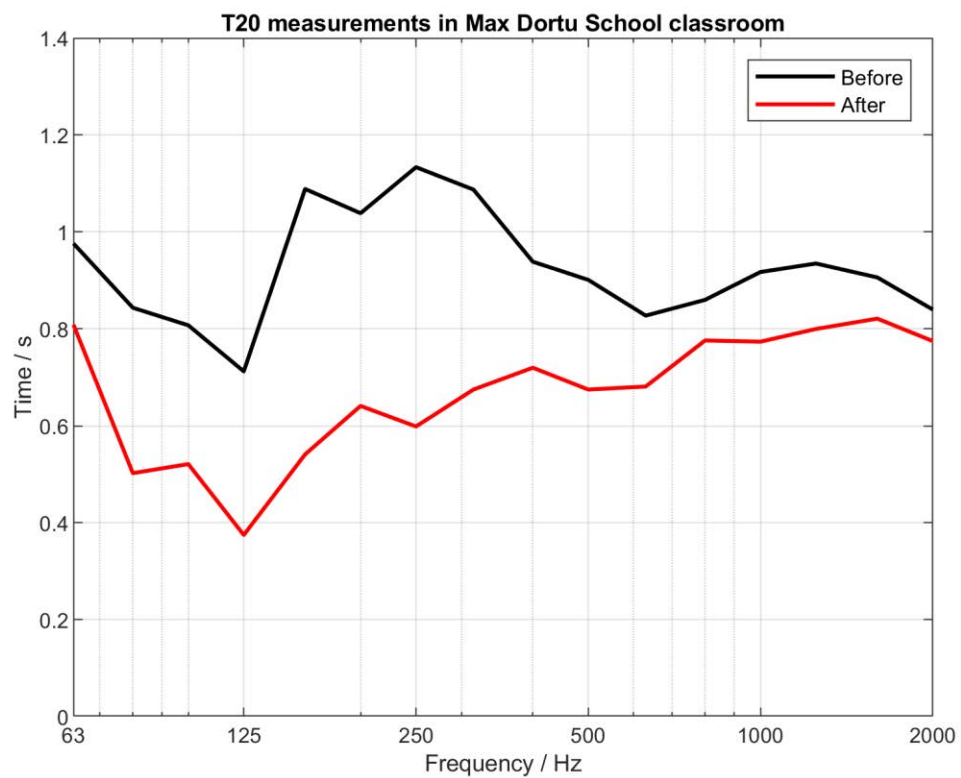
Figure 34. Measured reverberation times of a 123.1 m³ classroom treated with 21 BAT modules before and after installation

3.3. Results of impedance tube measurements

The impedance tube measurements provided the possibility to observe the specific absorption properties of the individual sides of the BAT module, namely the smooth and perforated sides. Unlike the reverberation chamber measurements, the results do not show the average absorption coefficients of the entire BAT, rather the absorption caused by the responsible physical mechanism. The data below shows the calculated absorption coefficients from the measured reflection factors for the smooth and perforated sides with a 0, 10, and 20 cm air cavity below the absorber, as well as the impedance for the same.

First, Figure 35 shows that maximal absorption of the smooth side of the BAT module is found, similarly to the reverberation chamber measurements, between 50 and 315 Hz. Local maxima of the peaks at the lower part of the spectrum shift to lower frequencies as the height of the air cavity below the absorber is increased. The increase in absorption above 315 Hz is unexpected, and is presumably the result of air slits around the edges of the absorber caused by the presence of mounting screws, which allow sound waves to penetrate along the sides of the tube thus providing access of the incident sound wave to the perforated faces.
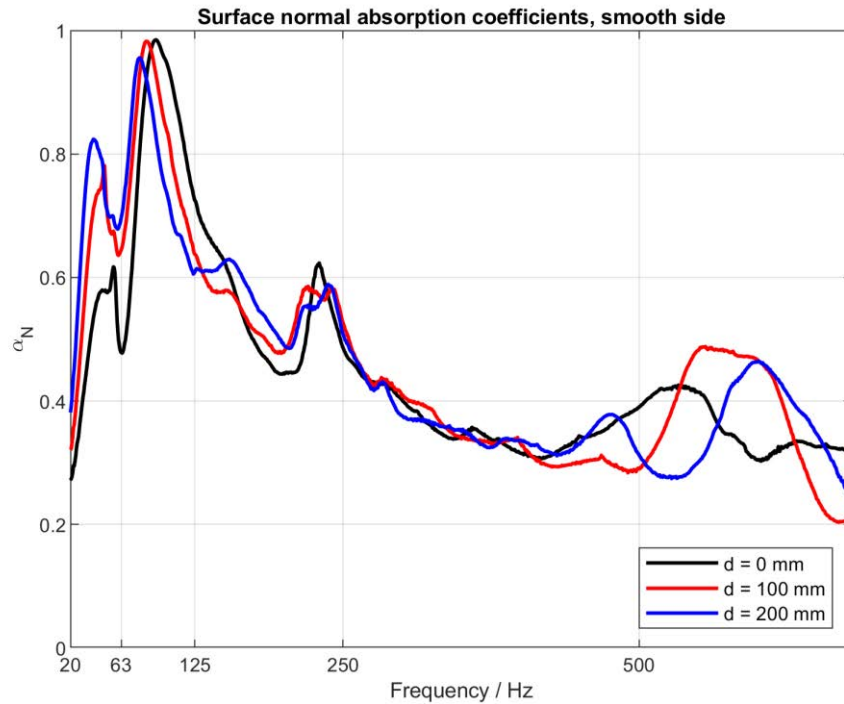
Figure 35. Absorption coefficients of smooth side of the BAT module obtained from impedance tube measurements with a 0, 10, and 20 cm air cavity between absorber and sound hard end of tube.

As the analytical calculations will later reflect, the absorption coefficients obtained from measurements of the perforated surfaces (see Figure 36 below) of the absorber display high levels of absorption (.7-.9) above 80 Hz. Once again, local maxima occur at and below 125 Hz, decreasing with frequency with increasing air cavity height.
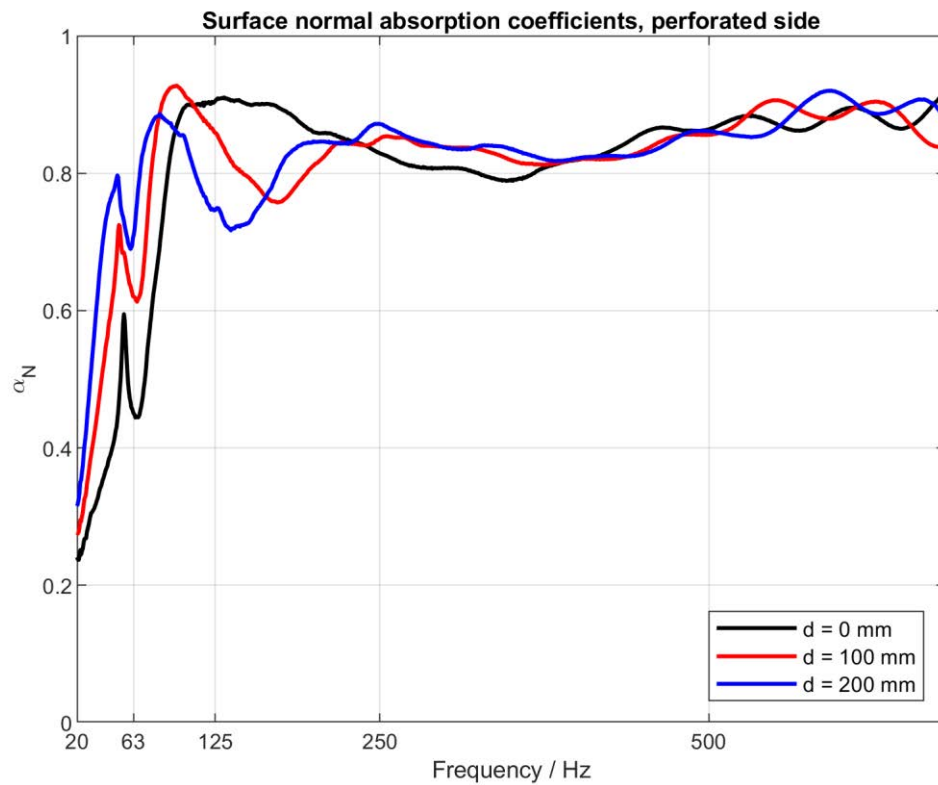
Figure 36. Absorption coefficients of perforated side of the BAT module obtained from impedance tube measurements with a 0, 10, and 20 cm air cavity between absorber and sound hard end of tube.

The impedance normal to the absorber surface was measured and calculated, for all six measurement configurations. Figure 37, Figure 38, and Figure 39 show the results according to the air cavity size below the absorber module. In each figure, both the real and imaginary parts of the normalized impedance are shown.

In all three situations (d = 0, 10, and 20 cm), the acoustic resistance of the smooth side generally sees a minimum around 63-80 Hz, and tends to increase with decreasing frequency, and increase as it approaches 400 Hz. This indicates higher energy losses at the minimum, as waves will more strongly reflect as the acoustic resistance increases.
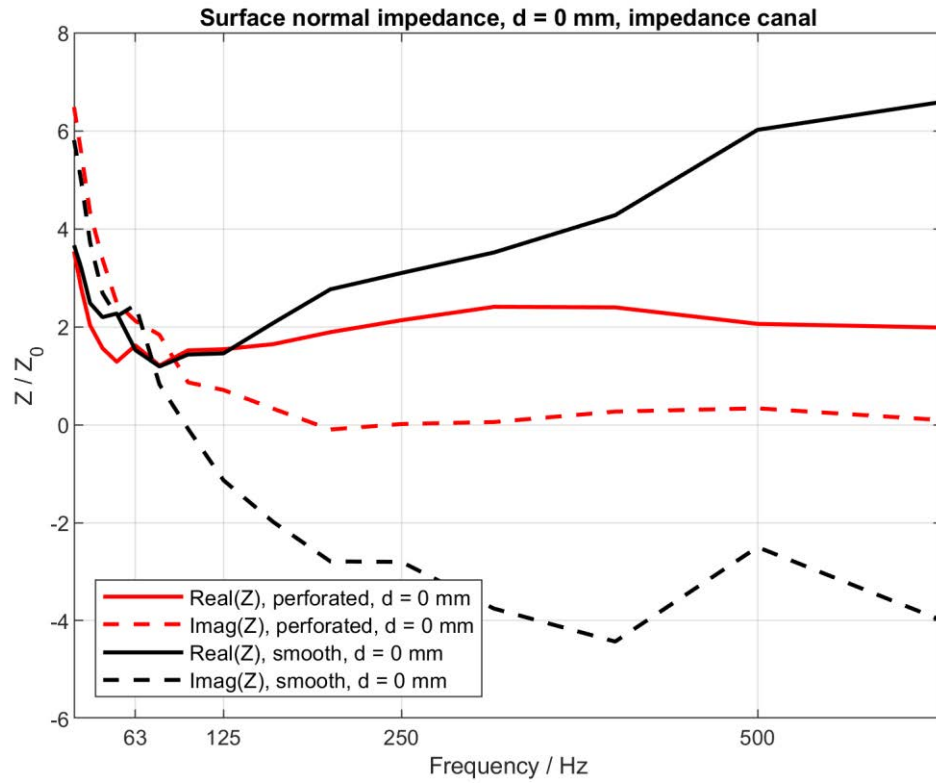
Figure 37. Impedance of smooth and perforated sides of BAT with no air cavity below, measured in impedance tube
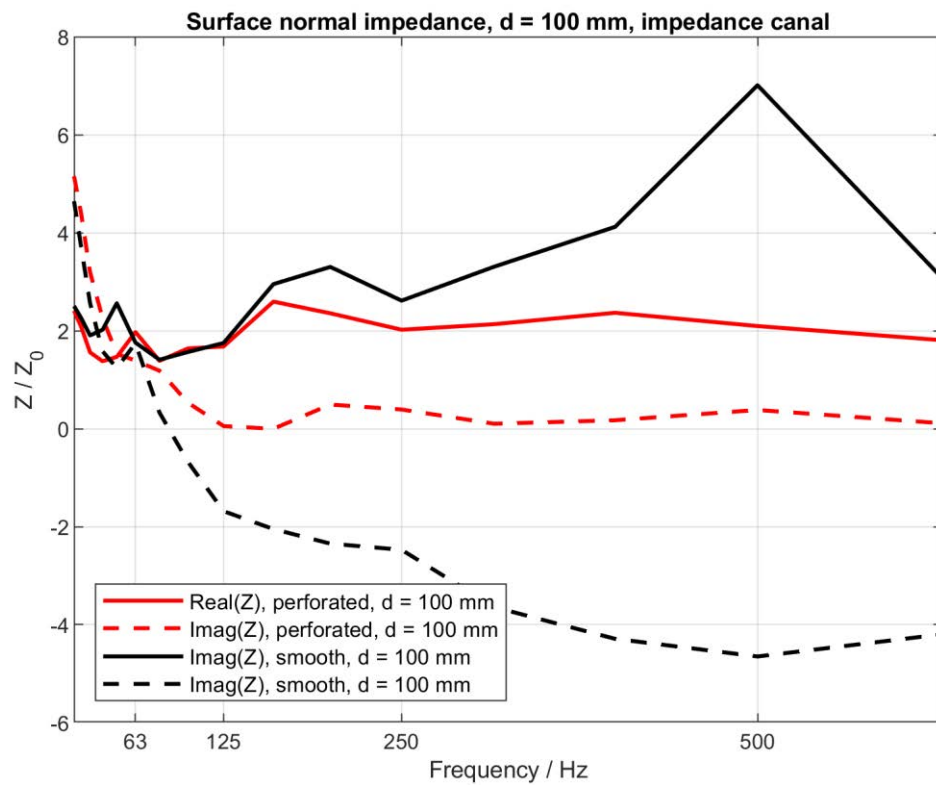
Figure 38. Impedance of smooth and perforated sides of BAT with 100 mm air cavity below module, measured in impedance tube
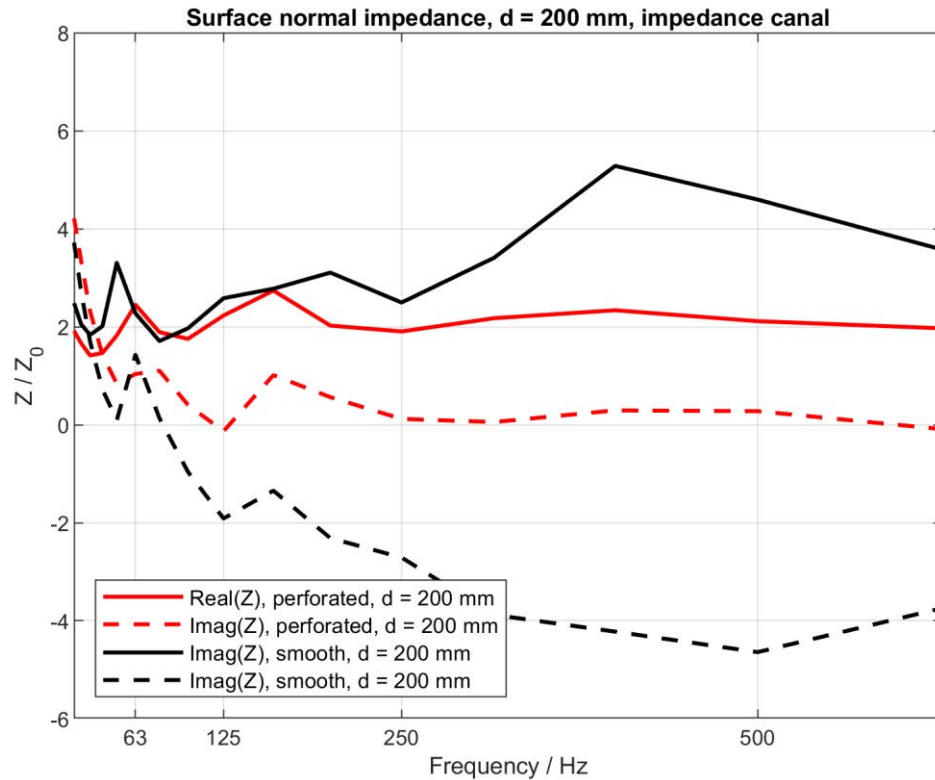
Figure 39. Impedance of smooth and perforated sides of BAT with 200 mm air cavity below module, measured in impedance tube

Interestingly, the acoustic resistance of the perforated side remains fairly constant above 250 Hz and sits well below the resistance of the smooth side. Even here, minima may be found between 30 and 80 Hz, whose position tends to shift towards lower frequencies as the volume of the air cavity is increased, for both the smooth and perforated sides. This seems to indicate that the BAT is most efficient in transforming sound energy between ca. 30 and 100 Hz. The reverberation chamber measurements, in contrast, showed the highest absorption at 125 Hz.

3.4. FEM simulation results of BAT absorption properties

An FEM simulation of the BAT in 3D space allowed for the calculation of the reflection factor *R,* from which the absorption coefficients could be derived via equations 2.5.8. for *R* and analogue to the impedance tube measurements, 2.4.14 for *α*. The results of the smooth side simulation shown below in Figure 40 resemble conventional plate resonator absorption characteristics, with a narrow band of efficiency centered around a resonance frequency, namely 40, 35.5, and 31.5 Hz for 0, 10 and 20 cm respectively, dictated by the plate thickness and density, damping material characteristics and depth, as well as the air cavity depth beneath the bottom plate.
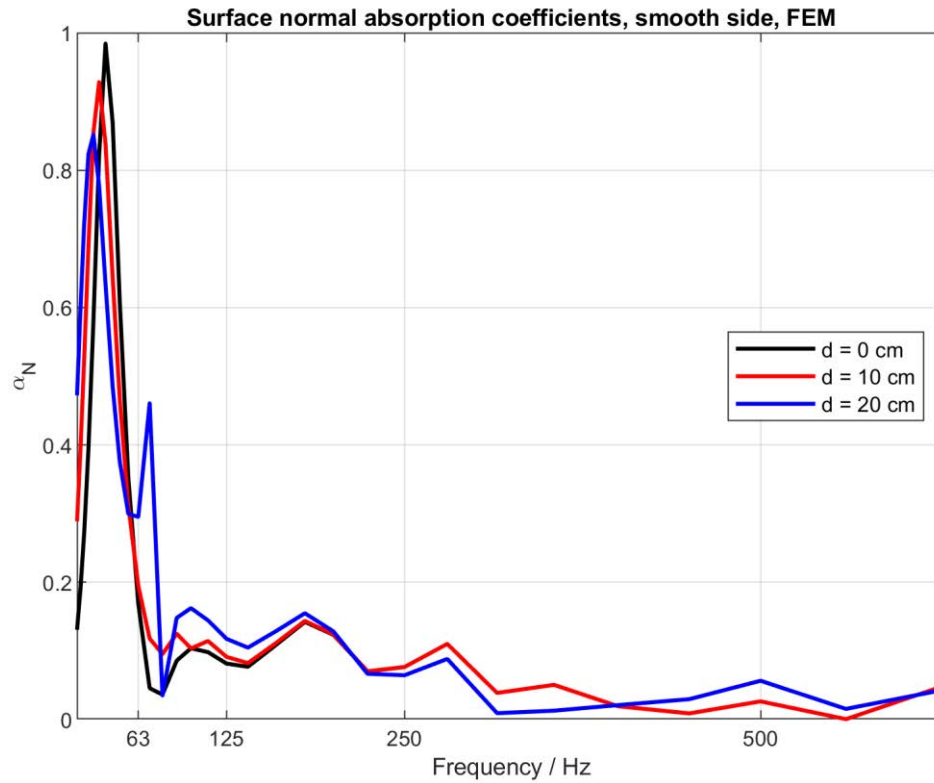
Figure 40. Simulated absorption coefficients of smooth side of the BAT with a 0, 10, and 20 cm air cavity between absorber and sound hard end of modelling domain.

Similar to the results of the smooth side simulations, the simulation of the perforated side of the absorber module shows general absorption characteristics representative of the results obtained from the impedance tube measurements. In figure Figure 41, it is shown that absorption rapidly increases between 0 and

125 Hz, and wavers around a maximum value of 0.9 with increasing frequency, increasing only slightly towards 630 Hz.
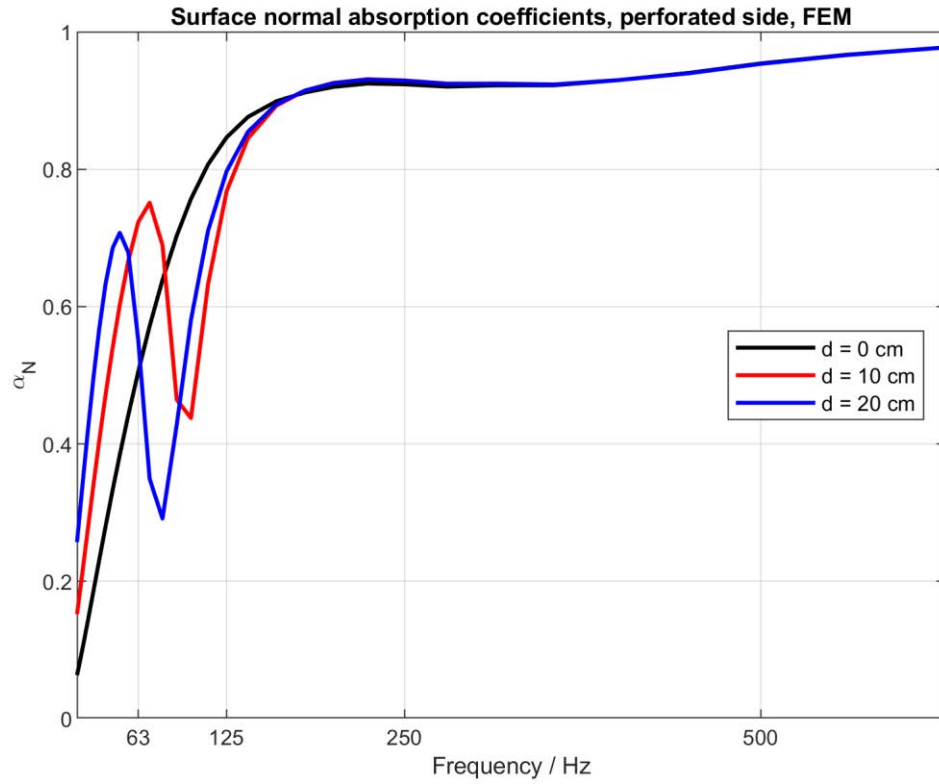
Figure 41. Simulated absorption coefficients of perforated side of the BAT with a 0, 10, and 20 cm air cavity between absorber and sound hard end of modelling domain.

The local maxima found at 71 and 50 Hz for the 10 and 20 cm air cavity configurations are likely a result of resonances occurring between the bottom smooth plate and the sound hard end of the modelling domain.

At first glance, the calculations of the impedance of the smooth side shown in Figure 42 seem to provide undetailed information. The results show low resistance and reactance below 300 Hz, with significant local maxima for all air cavity sizes in both the real and imaginary parts of the impedance above 300 Hz. This part of the frequency range is, however, of lesser interest for this study than the values which are achieved below 300 Hz. However, rescaling and zooming in on the data below 160 Hz provides much more useful information, as seen in Figure 43. Here, we see a more detailed view of the zero-crossings of the imaginary part of the impedance, again identifying resonant frequencies which

tend to sink with increasing air cavity depth. Absolute values of the resistance magnitudes increase above and below 100 Hz, with local maxima around the plate resonant frequencies.
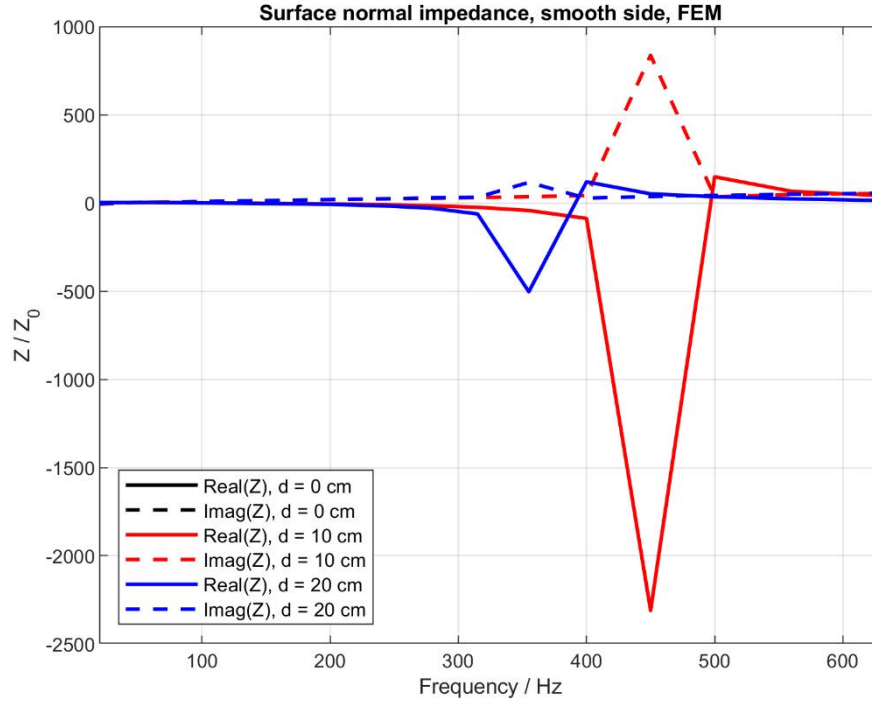
Figure 42. Simulated impedance of smooth side of BAT for 0, 100, and 200 mm air cavity model configurations
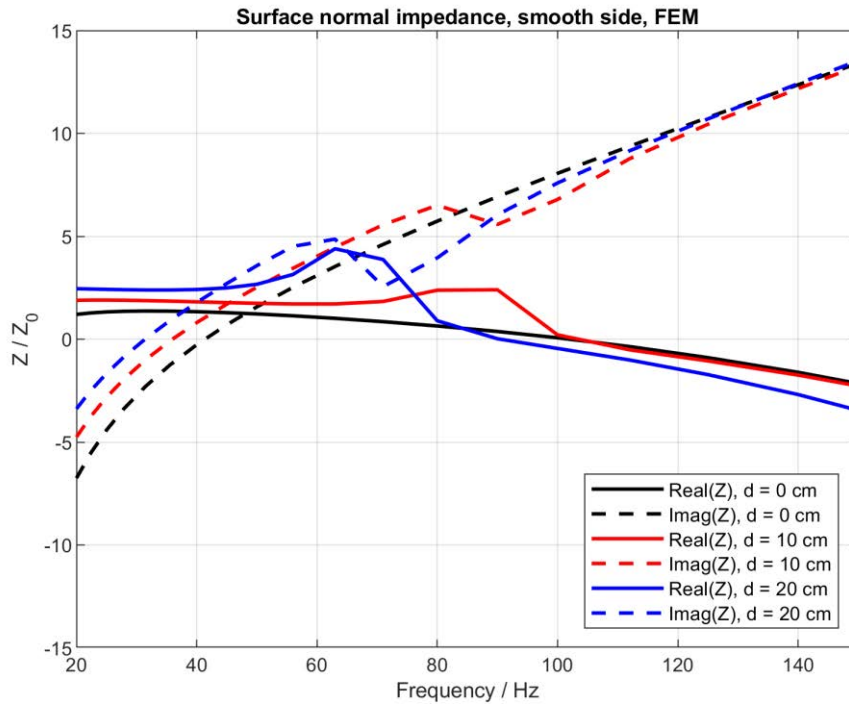
Figure 43. Simulated impedance of smooth side of BAT for 0, 100, and 200 mm air cavity model configurations, plot detail

A global view of the surface normal impedance calculation of the perforated side initially shows no resonant frequencies. There are no zero-crossings in the imaginary parts of the individual simulations, though it can generally be said that reactance decreases with increasing frequency, with local minima of the absolute values, indicating a rapid phase shift towards a decreased offset centered around frequencies which could be interpreted as plate resonances within the perforated plate, although the imaginary part is not equal to zero. It is more likely however, that the perforated plates do not resonate, and the porosity and hole size of the plates allow for air particles to freely enter the porous material, as if the plate was not even there. In this sense, the perforated side shows the absorption characteristics of the porous material, in this case mineral wool.
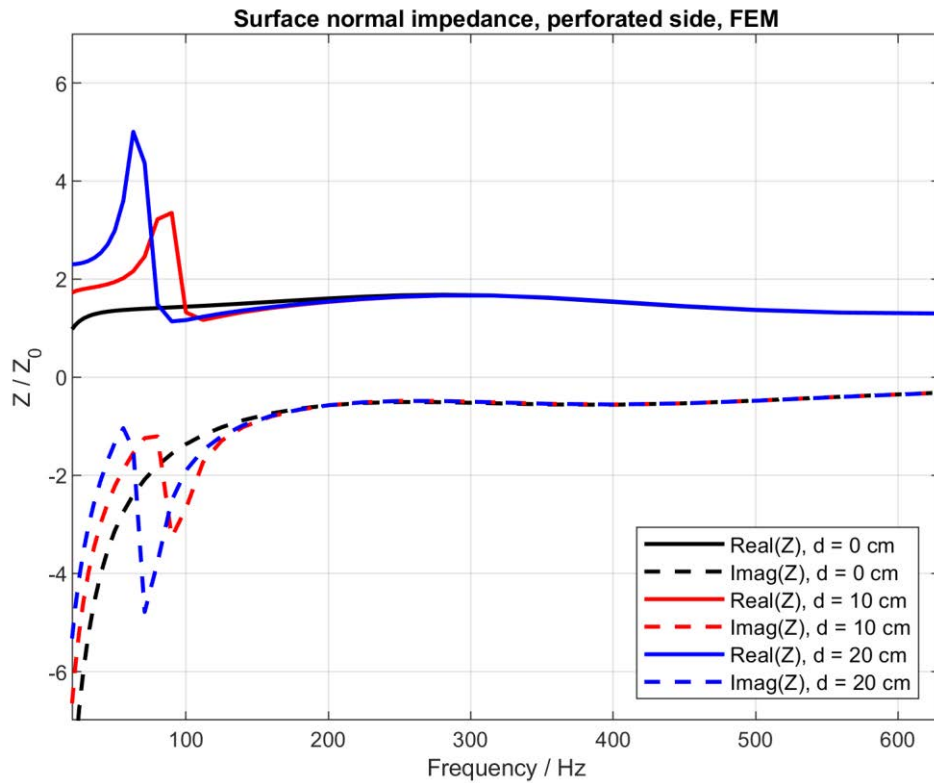
Figure 44. Simulated impedance of perforated side of BAT for 0, 100, and 200 mm air cavity model configurations

The reactance encounters local maxima around the same respective frequencies, all of which are below 100 Hz. This indicates an abrupt physical change in the absorption mechanism active around those frequencies, namely from porous absorption to damped plate resonator. Again, this is most likely due

to the presence of the smooth plate on the underside of the simulated absorber module.

3.5. Results of FEM room simulation

For each of the 21 models, the direct frequency response was calculated at 1344 positions of a 28 x 48-point array at a height of 1.2 m within the room. The initial results were calculated with a frequency range from 20 to 630 Hz with a 1/6th octave frequency resolution. Since 630 Hz is well above the modal frequency range, it was necessary to find a frequency range better fit to the study. In order to find this, the standard deviation was calculated with increasing frequency range included in the calculation. Plotting the deviation against upper inclusion frequency limit allowed for the identification of the upper limit after which the deviation was no longer greatly affected by increasing the range. Calculated for the undamped room, the results are shown in Figure 45, and it shows that around 160 – 170 Hz the results flatten out. Based on this, the limit of 165 Hz was chosen as the upper frequency range for the study.
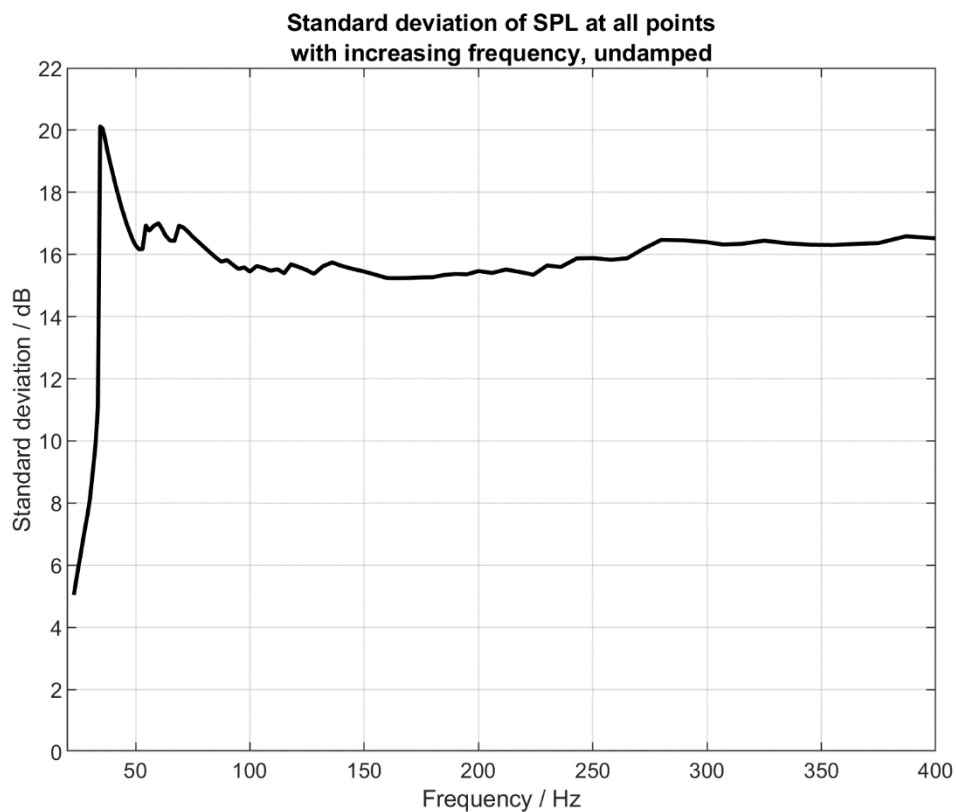
Figure 45. Standard deviation over the entire space plotted against upper frequency limit included in the calculation

Generally, it is not possible to optimize the frequency response for the entire room, which is why the results were broken into three categories, namely optimization in the front, middle, and back sections of the room. The standard deviation at all points in the array was calculated and visualized in image plots representing the horizontal plane containing the sampling array. The front wall of the room where the source was defined is at the bottom of the plot. Shown below in Figure 46 are the results for the undamped room, followed by the results of the configurations which most optimized the frequency response in either the front, middle or back sections of the room. The remainder of the results may be found in the appendix.
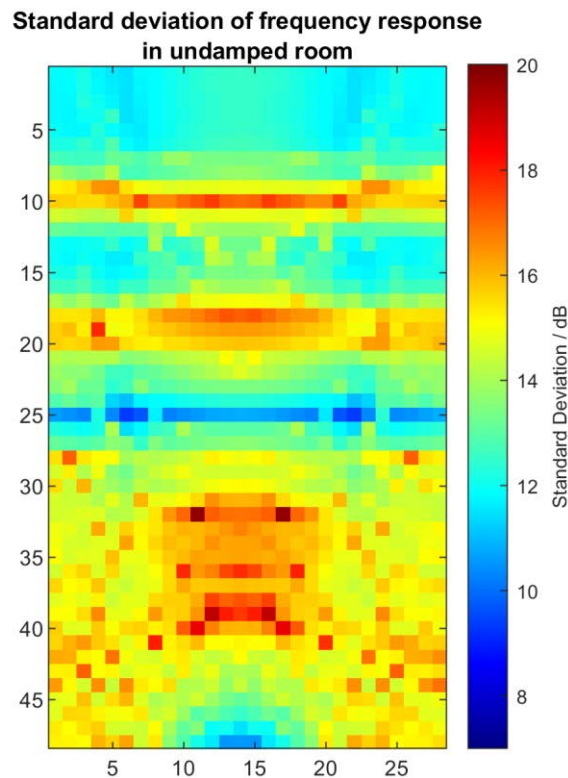
Figure 46. Standard deviation of frequency response at all sampling points in undamped room

In the undamped room, it is quite clear that the frequency responses are subject to higher ranges of deviation in all parts of the room, excluding a limited area across the center horizontal axis in the plot. In the front part of the room, the deviation ranges from 10.8 to 19.7 dB. The middle section of the room is subject to a deviation of 9.3 to 17.8 dB, while in the back part the deviation ranges from

11.5 to 17.6 dB. The results of the configuration which most optimized the front section of the room, seen here in Figure 47, corresponds to configuration shown to the left of the plot. The frequency response deviation in the front of the room is shown to be reduced to 7.5 to 9.5 dB, as opposed to 10.8 to 19.7 dB. Interestingly, optimizing the front of the room comes at the cost of a significant increase in deviation in the back of the room, seeming to polarize the room.
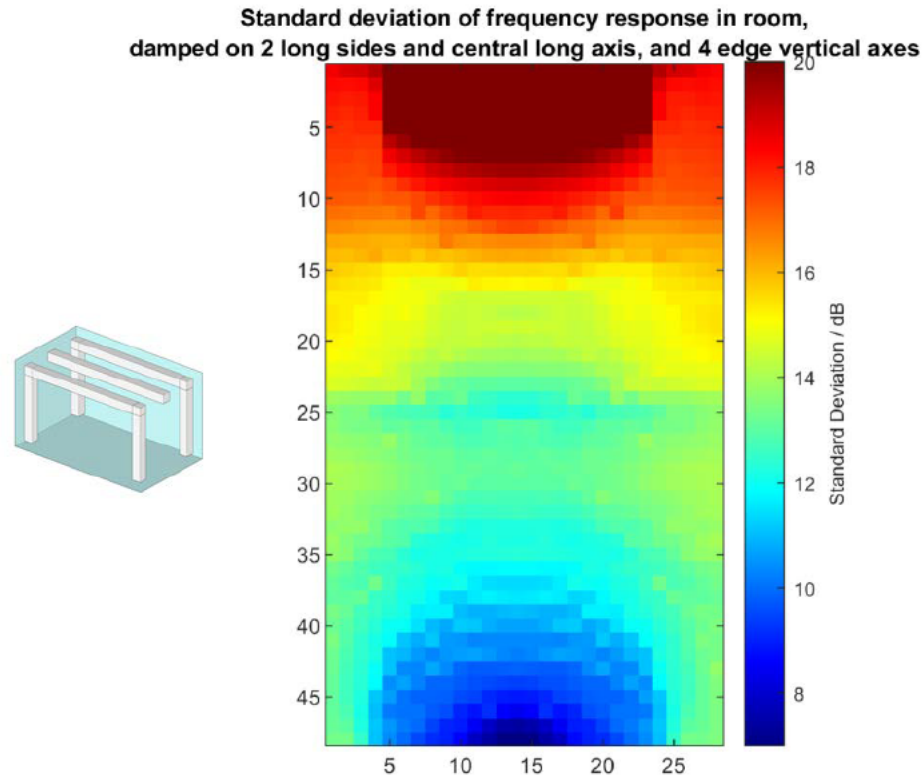
Figure 47. Standard deviation of frequency responses at all sampling points, front section optimized, shown with corresponding absorber module configuration.

The results from the optimized middle section of the room, shown in Figure 48 with the corresponding absorber module configuration, shows a decrease in standard deviation across the horizontal middle axis of the room, with a deviation range of 8 to 10 dB, compared to the 9.3 to 17.8 dB range of the undamped room. In this case, significant improvements can also be found within the front section of the room as well.
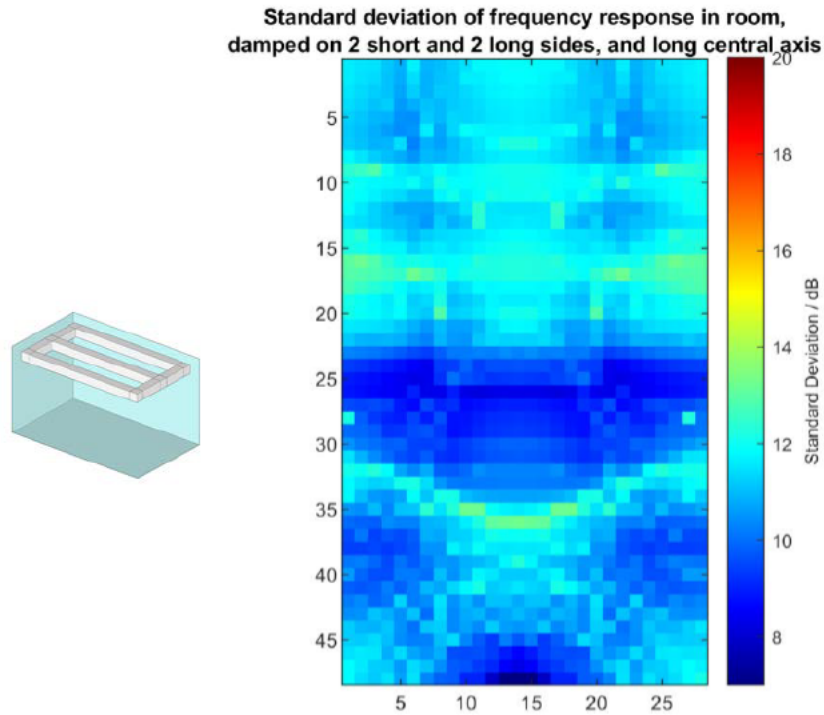
Figure 48. Standard deviation of frequency responses at all sampling points, middle section optimized, shown with corresponding absorber module configuration.

In Figure 49, the entire back half of the room is shown to have improved, with the greatest reduction in frequency response deviation contained to the anterior 3 m^2 ranging from 6.5 to 11.5 dB, compared to the 11.5 to 17.6 dB range in the undamped room model, simply by damping the short upper edges of the room.
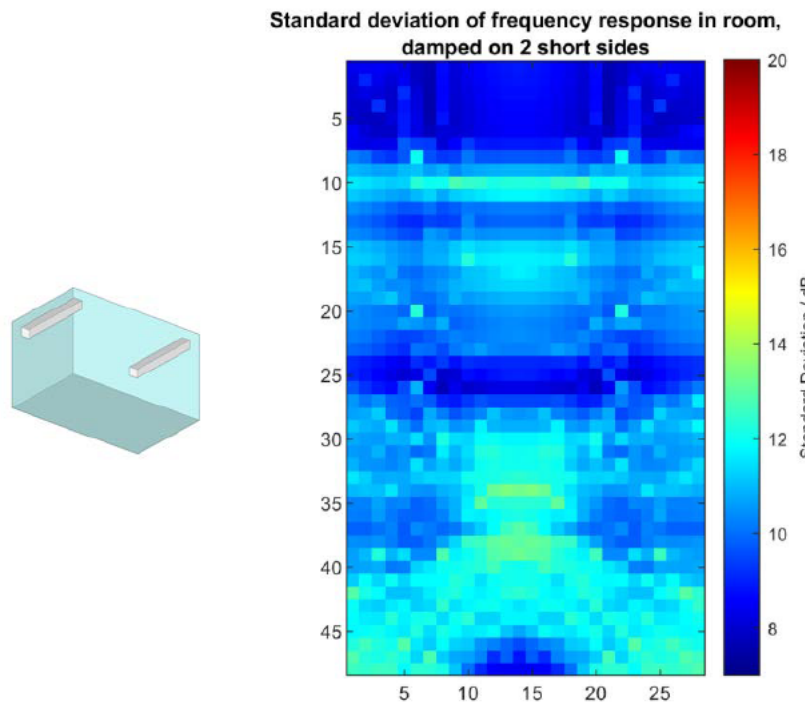
Figure 49. Standard deviation of frequency responses at all sampling points, back section optimized, shown with corresponding absorber module configuration.

4. Analysis of results

In this section, the results of the various measurements and simulations will be compared and discussed in order to correlate the findings. The reverberation chamber measurements will be compared to the sample room measurements, while the impedance tube results will be discussed in relation to the FEM simulation and an analytical model which will be presented here. Finally, the results of the room simulation will be further analyzed and quantified statistically, while the changes to the sound field will be discussed in terms of the governing equations.

4.1. Absorption coefficients derived from sample room and reverberation chamber measurements

The absorption coefficients for the absorber modules resulting from the reverberation chamber measurements should be able to be used when planning the number of BATs needed to obtain a desired reverberation time in rooms to be treated. Comparing the absorption coefficients from the reverberation chamber to the sample rooms gives an indication to the accuracy with which a treatment may be planned. Calculating the absorption coefficients based on the sample room measurements is done using the following equations:

the aequivalent absorption prior to renovation,

$$A_{before} = 0.163 * \frac{V}{T_{before}} \ [\mathrm{m^2}] \qquad (4.1.1)$$

the aequivalent absorption after BAT installation in m2,

$$A_{after} = 0.163 * \frac{V}{T_{after}} \ [\mathrm{m^2}] \qquad (4.1.2)$$

The change in aequivalent absorption surface area, giving the A_{eq} per BAT,

$$\Delta A = \frac{1}{N}(A_{after} - A_{before}) \ [\mathrm{m^2}] \qquad (4.1.3)$$

where *N* = the number of implemented modules, and finally

$$\alpha = \frac{\Delta A}{S_{BAT}} \qquad\qquad (4.1.4)$$

gives the derived absorption coefficients of BATs measured in situ where S_{BAT} is the surface area of one module.

Figure 50 shows the results of this calculation, filtered to octave bands.
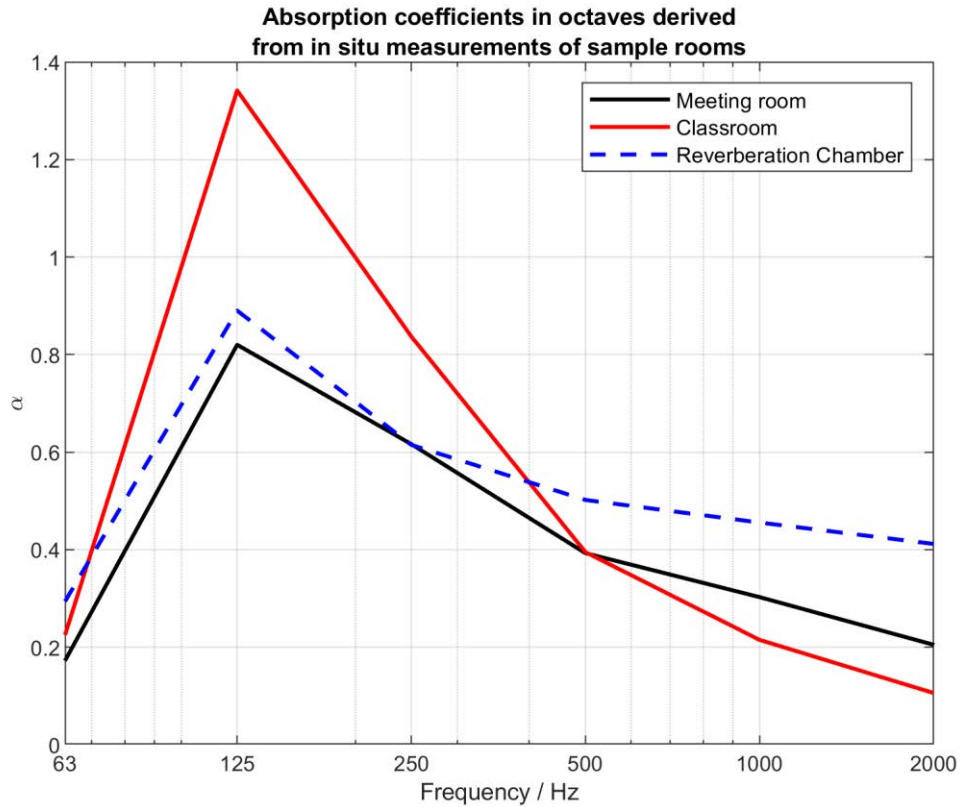
Figure 50. Absorption coefficients of BAT units calculated from T20 measurements of sample rooms compared to reverberation chamber measurement results

As shown in the plot, the in-situ measurements are consistent with the expectations of the reverberation chamber measurements, in that maximum absorption occurs at 125 Hz, reducing to moderate absorption at lower and higher frequencies. There is good agreement between the results of the meeting room and reverberation chamber measurements below 250 Hz, however the coefficients derived from the classroom measurements seem to overshoot the expectations by about .4. This is not entirely unsurprising, given that the initial reverberation chamber measurements also show absorption coefficients greater than 1 before being averaged, from which the meeting room calculation shown

above does not greatly deviate. Based on this, it can be said that the absorption coefficients based on the reverberation chamber measurements are a good indication of what one could expect with an implementation of a set of BAT modules, providing a decent amount of accuracy for predicting the resulting reverberation times. Additional sample room measurements would be necessary however to further confirm that.

4.2. Analysis of impedance tube measurements

To give a sense of the overall tendencies of the acoustic reactance properties of the BAT, the imaginary part of the normal impedance has been plotted in Figure 51 for all measurements in a single graph. One sees immediately that the smooth sides always have single zero-crossings below 100 Hz for each measurement, while the perforated sides cross more than once, and generally at a higher frequency. This may be a result of plate resonances occurring on the anterior side of the BAT within the impedance tube. A more detailed inspection of the behavior of the smooth side shows the role of the air cavity on the resonant frequency, as presented in Figure 52.
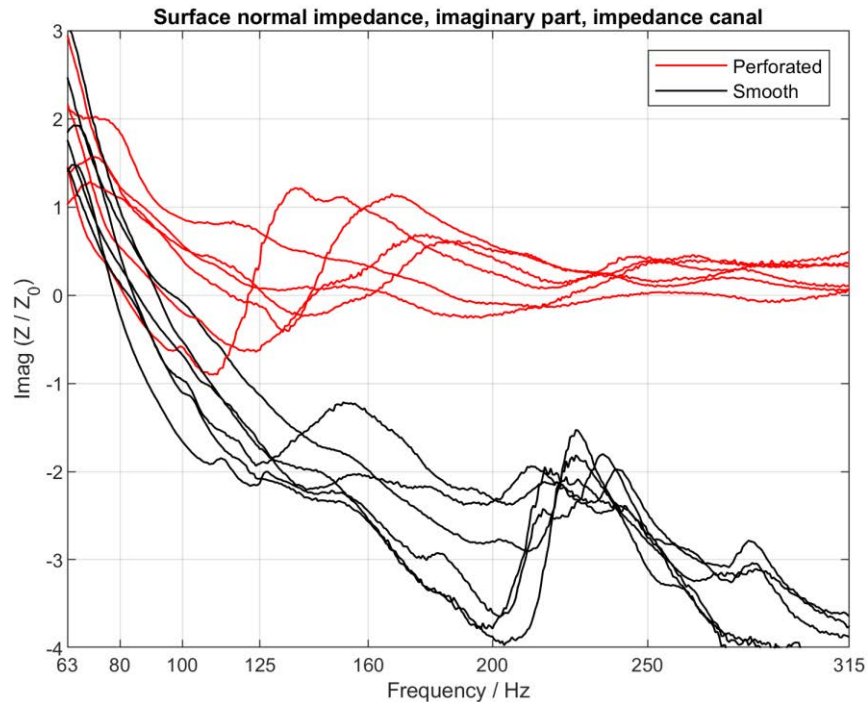
Figure 51. Imaginary parts of impedances measured in impedance tube, for smooth and perforated sides for all air cavity sizes

71
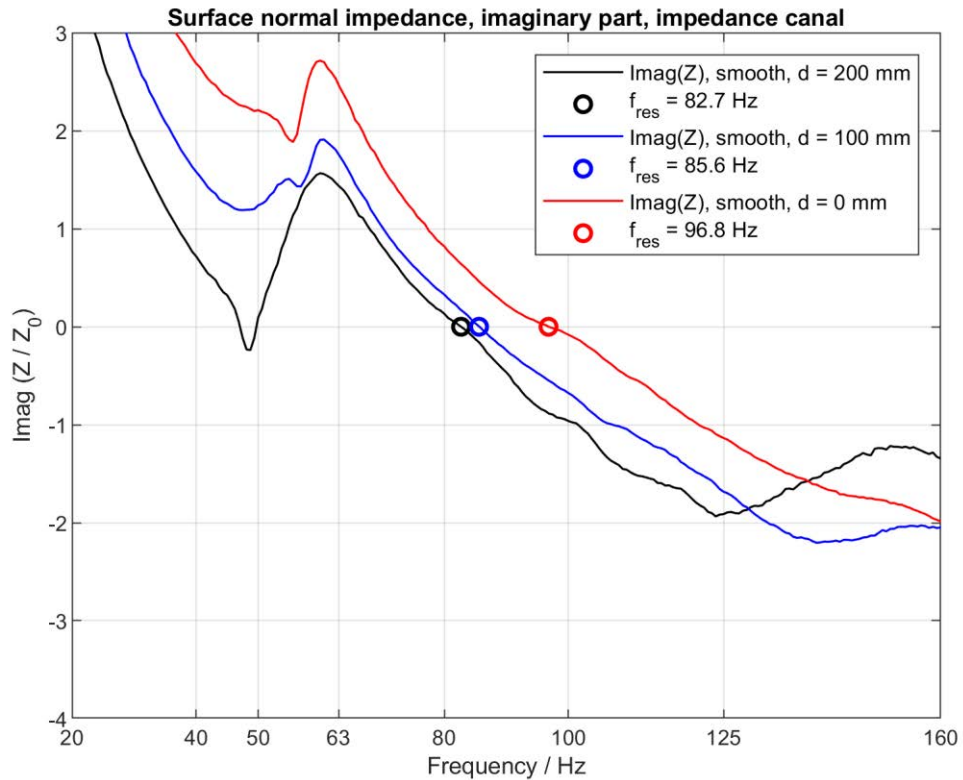
Figure 52. Location of resonant frequency for the smooth side for all air cavity sizes

This graph allows for the identification of the resonant frequency per configuration. The lowest resonant frequency occurs at 82.7 Hz when the module is placed 200 mm from the wall, increasing to 85.6 Hz when the air cavity is decreased to 100 mm. No air cavity results in a resonant frequency of 96.8 Hz.

Using this information, as well as the data shown in Figure 50, the resonant behavior of the entire module as a result of air cavity size may be observed by plotting the resonant frequency for each side over the air cavity size, as seen in Figure 53. Here, it is shown the resonant frequency sinks with increased distance to the wall. The curves labelled "second set" and "first set" derived from the measurements of the perforated side, are again most likely a result of plate resonances within the smooth side plate of the BAT facing the wall.
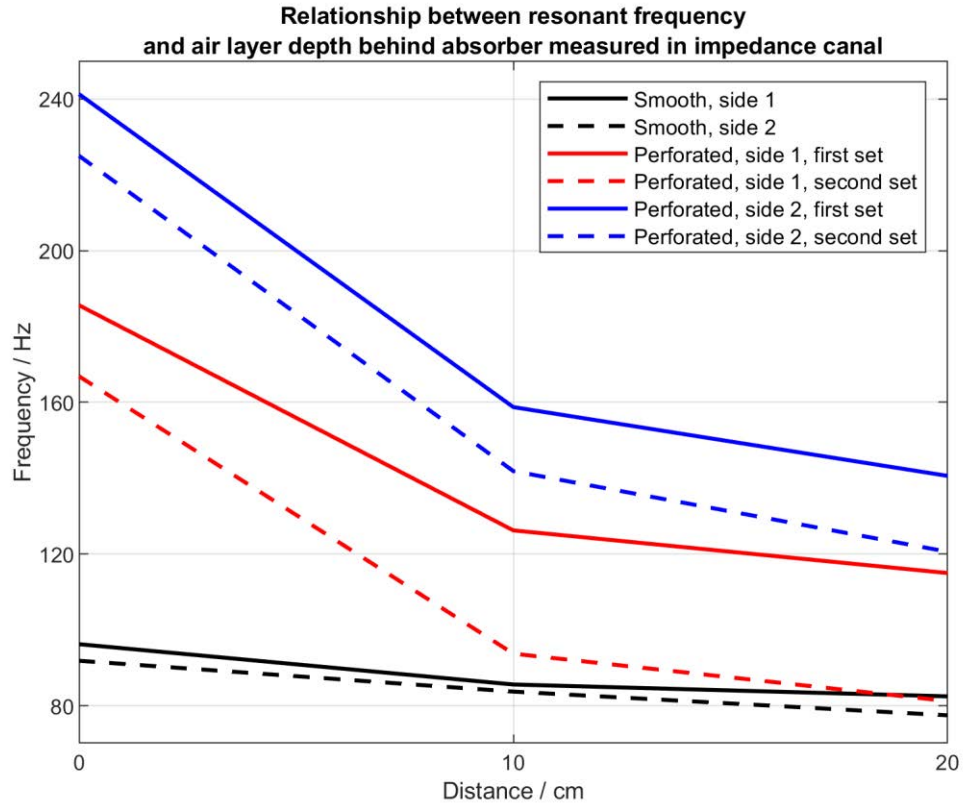
Figure 53. Resonant frequency derived from impedance tube measurements for all sides and air cavity sizes, as it sinks with increasing air cavity size

Taking a weighted average of the absorption coefficients from the impedance tube measurements allows for a comparison with the coefficients from the reverberation chamber tests. This is done however with caution since the absorption coefficients found in the impedance tube measurements are the *normal* absorption coefficients, while the latter are the statistical (diffuse field) coefficients. The averaged coefficients were calculated with the following formula:

$$\alpha_{ave} = \frac{S_{perf}\alpha_{perf} + S_{smooth}\alpha_{smooth}}{S_{perf} + S_{smooth}} \qquad (4.2.1)$$

where S_{perf} is the total surface area of the perforated plates on the module, S_{smooth} is the total surface area of smooth perforated plates on the module, and α_{perf} and α_{smooth} the respective averaged absorption coefficients for each side found from the impedance tube tests.

Though general agreement regarding the behavior may be found, the greatest discrepancy lies in the location of greatest absorption as seen in Figure 54. The impedance tube results indicate that greatest absorption occurs at 89 Hz, while the reverberation chamber measurements show 125 Hz. The difference may be

a result of the significantly different measuring methods and nature of the absorption coefficient type.
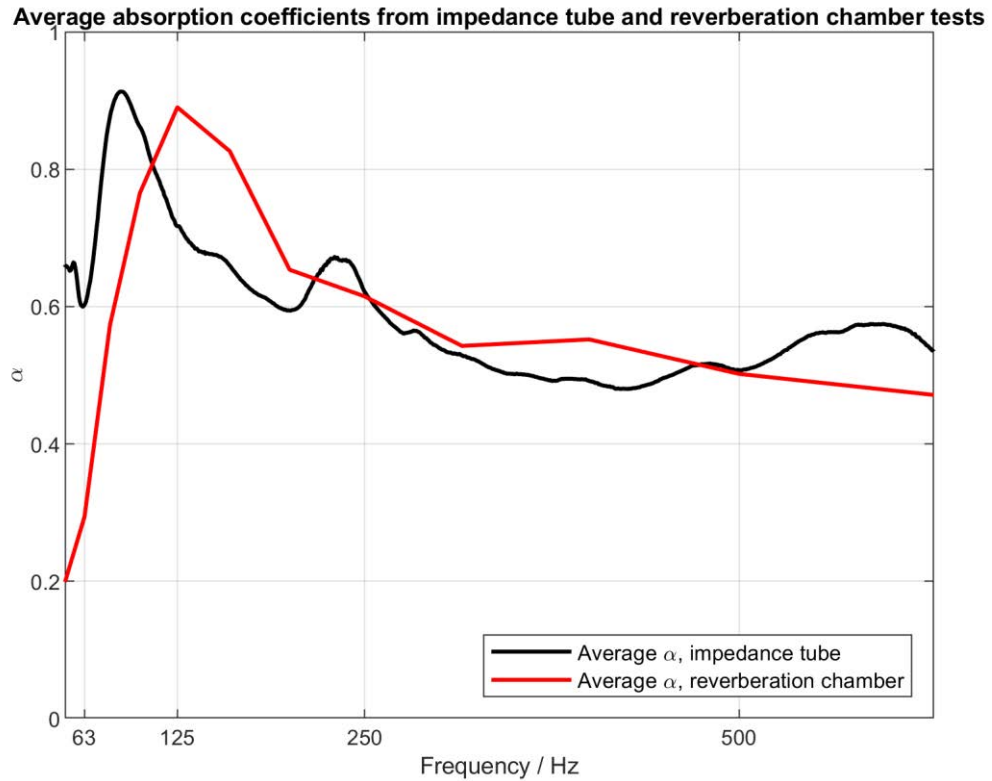
Figure 54. Comparison of average absorption coefficients calculated from impedance tube and reverberation chamber test results

4.3. Numerical results compared to analytical model and empirical results

Since the BAT consists of two different surface types, an individual analytical solution must be found for both surface types.

The impedance of the smooth surface may be found using an idealized model, with the assumption that the unit is placed directly in front of a sound hard wall, and that each layer of the structure parallel to the wall extends infinitely in two dimensions. Additionally, it is assumed that the surface is subject to plane wave irradiation perpendicular to the wall. This side will be described using equations for a damped membrane absorber.

As no exact analytical solution exists for finding the surface impedances of the perforated surface, an approximation using a transfer matrix method was used to

find the idealized surface impedance of the structure in front of a sound hard wall. The assumptions here are the same as above.

The benefit of using the transfer matrix method is that a larger number of geometrical and material parameters may be used and accounted for when defining the surface impedance of individual layers. Essentially, the transfer matrix method calculates the surface impedance of each layer, providing an input impedance for the subsequent layer, and taking the sum of the individual impedances to find the total normal impedance of the unit.

Given the perforation size, layer thickness, and porosity of the perforated plate, the impedance of the perforated plate size depends primarily on the properties of the porous material, and ultimately acts as a porous absorber since air particles may freely enter and exit the perforations without significant compression. Beginning with the transfer matrix method equations for the perforated plate, the impedance is defined as follows:

$$Z_{s1} = -jZ_c \cot(k_1 d) \tag{4.3.1}$$

describes the impedance directly behind the perforated sheet, namely in front of the porous material, while

$$Z_c = \rho_0 c (1 + 0.0571 X^{-0.754} - j0.087 X^{-0.732}) \tag{4.3.2}$$

with

$$X = \frac{\rho_0 f}{\Xi} \tag{4.3.3}$$

gives the characteristic impedance of porous absorber (Delany-Bazley, 1970) and

$$k_1 = \frac{\omega}{c}(1 + 0.0978 X^{-0.7} - j0.189 X^{-0.595})\frac{1}{m} \tag{4.3.4}$$

the characteristic wavenumber of porous absorber material (Delany-Bazley, 1970).

$\Xi = 5000$ Pa*s/m²; defines the fluid resistance of mineral wool used in the BAT. Taken together, the total impedance is calculated with

$$Z_{s2} = \frac{1}{\epsilon}(2\delta a + t) j\omega \rho_0 + Z_{s1} \tag{4.3.5}$$

for the porous sheet, taking into account the effect of the open area in the metal, with

$t =$ 0.7 mm; the thickness of metal plate

$a =$ 0.75 mm; the radius of perforation holes

$D =$ 3.5 mm; is spacing between perforation holes

$\epsilon = \frac{2\pi a^2}{\sqrt{3}D^2}$; as fraction of open area on porous sheet, and

$\delta = \frac{-1}{\pi} ln \left[sin \left(\frac{1}{2}\pi\epsilon \right) \right]$; being the end correction (Smits and Kosten, 1951), and finally the resulting absorption coefficients are given by

$$\alpha_{n,perf} = \frac{4\rho_0 c * Real(Z_{s2})}{(Real(Z_{s2}) + \rho_0 c)^2 + |Imag(Z_{s2})|^2} \tag{4.3.6}$$

(D'Antonio and Cox, 2017, section 7.3.3.3.)

The smooth side of the absorber, as stated above, is treated as a damped membrane or plate resonator and calculated by adding the impedance of the porous absorber material with the impedance of a non-perforated thin steel plate with

$$Z_{smooth} = Z_{s1} + jm''\omega \tag{4.3.7}$$

in which m'' = 7.8 kg/m² for steel. Again, the absorption coefficients are given by

$$\alpha_{n,smooth} = 4\rho_0 c \cdot \frac{Real(Z_{smooth})}{(Real(Z_{smooth})+\rho_0 c)^2 + Imag(Z_{smooth})^2}. \tag{4.3.8}$$

Shown together with the FEM calculation of the absorption coefficients, the analytical model may be compared with the numerical model as shown in Figure 55.
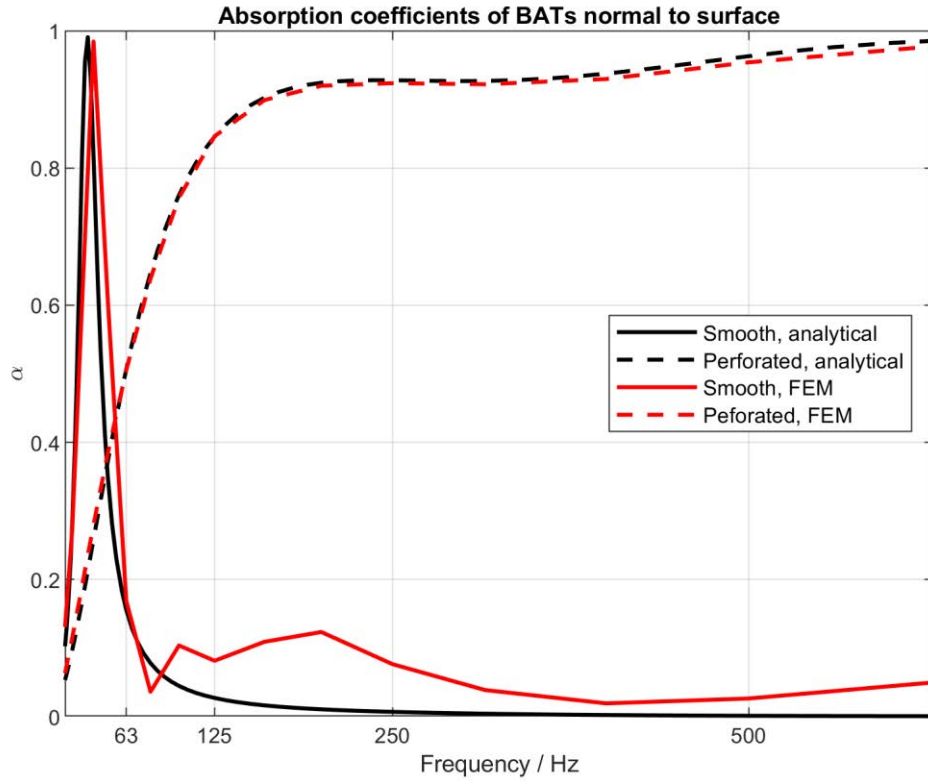
Figure 55. Comparison of the absorption coefficients calculated with the analytical model (black) and the numerical model (red) for both plate types and no air cavity behind absorber

Very good agreement may be seen for both sets of absorber coefficients, though the resonant frequency calculated in the analytical model is 5.4 Hz below that of the numerical model, 36 Hz and 41.4 Hz respectively. The agreement between the models is not entirely unsurprising since both are deterministic, depending on the same parameters. What is surprising however, is the low resonant frequency found in both models of the membrane resonator compared to the impedance tube measurements. This value is most greatly affected by the mass per unit surface area of the steel plate, which in actuality may differ from the theoretical assumption. Additionally, the way the real plate is mounted may also have an effect on the resulting resonant frequency, which in the case of the BAT is intermittent rivets.

The effect of the air cavity behind the absorber modelled numerically reflects the same behavior shown in the impedance tube measurements. Figure 56 shows the resonant frequencies for each air cavity size, in which we can see a decrease in frequency with increasing cavity depth by observing where the imaginary part

of the calculated impedance is equal to 0. Figure 57 shows the relationship explicitly, and parallels the empirical results shown in Figure 53.
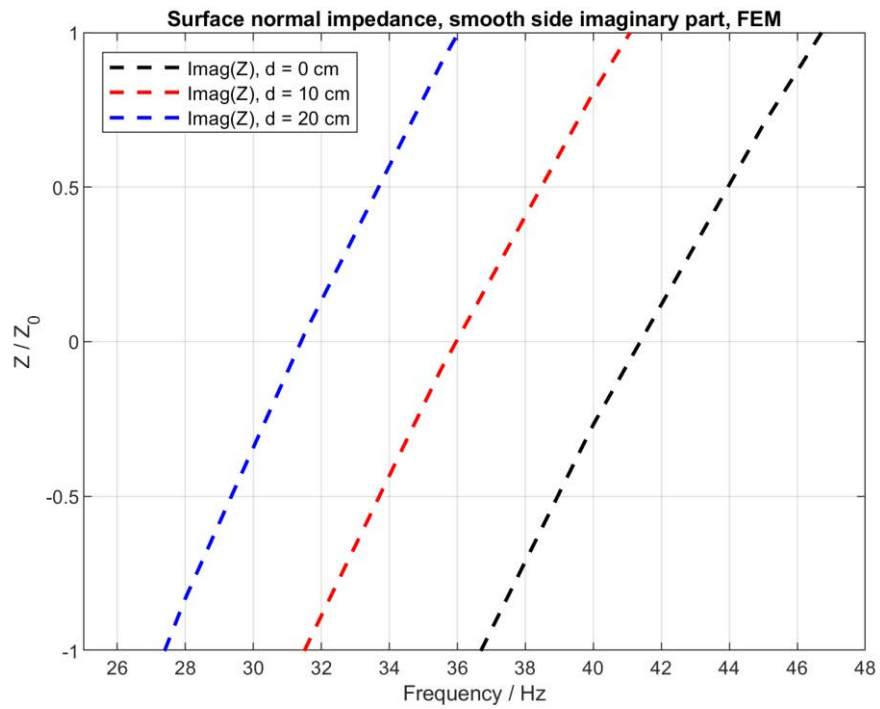
Figure 56. Imaginary part of the impedance of the smooth plate calculated numerically for all air cavity depths. The zero-crossing decreasing with cavity size increases shows the resonant frequency.
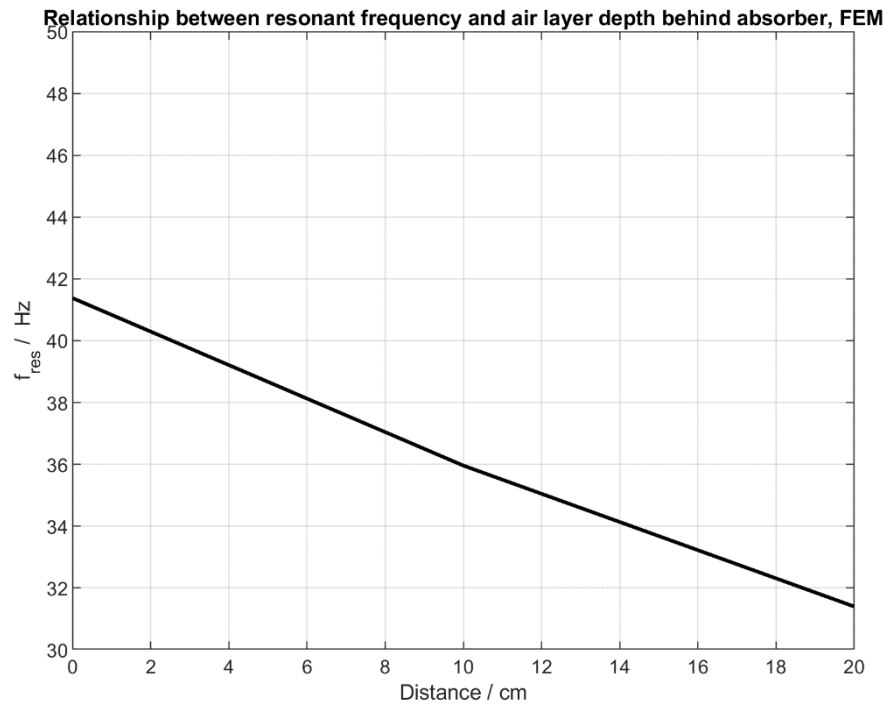
Figure 57. Resonant frequency of smooth plate calculated numerically with air cavity size

4.4. Analysis of room model calculations

The addition of damping volumes to the interior of the room model has clear effects on the resulting simulated sound field. By considering the frequency response at a given point with a defined source position, how can we observe more specific changes to individual room modes? One way to do this is by considering the average of all the frequency responses in a given section within the modelled space in both the undamped and damped space. For example, if we consider frequency responses only in the front part of the room, as shown in Figure 58, we immediately see the significant differences and tendency in the responses, as a result of damping with the configuration shown to the left of the figure.
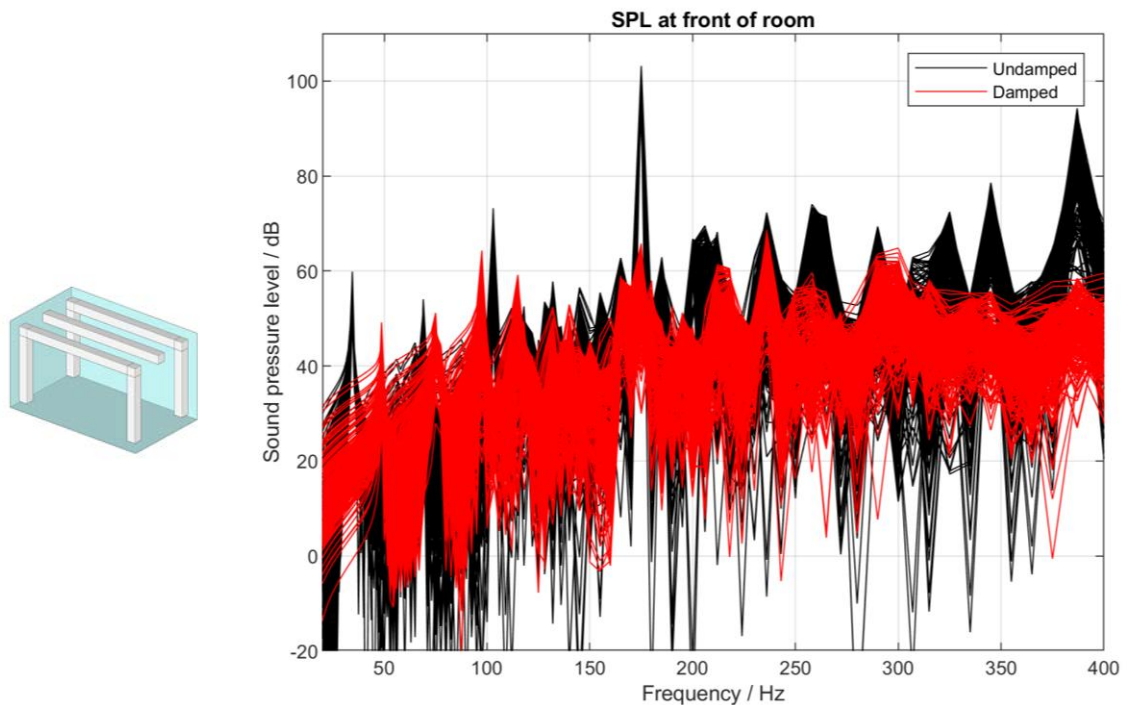
Figure 58. All frequency responses in front section of room in undamped (black) and damped (red) states

By taking the average of all the responses in each state, as shown in Figure 59, we begin to see how the frequency of the strongest modes are shifted and attenuated, signaling a stretching of the mode shape or compression, depending on whether the frequency decreased or increased respectively.

79
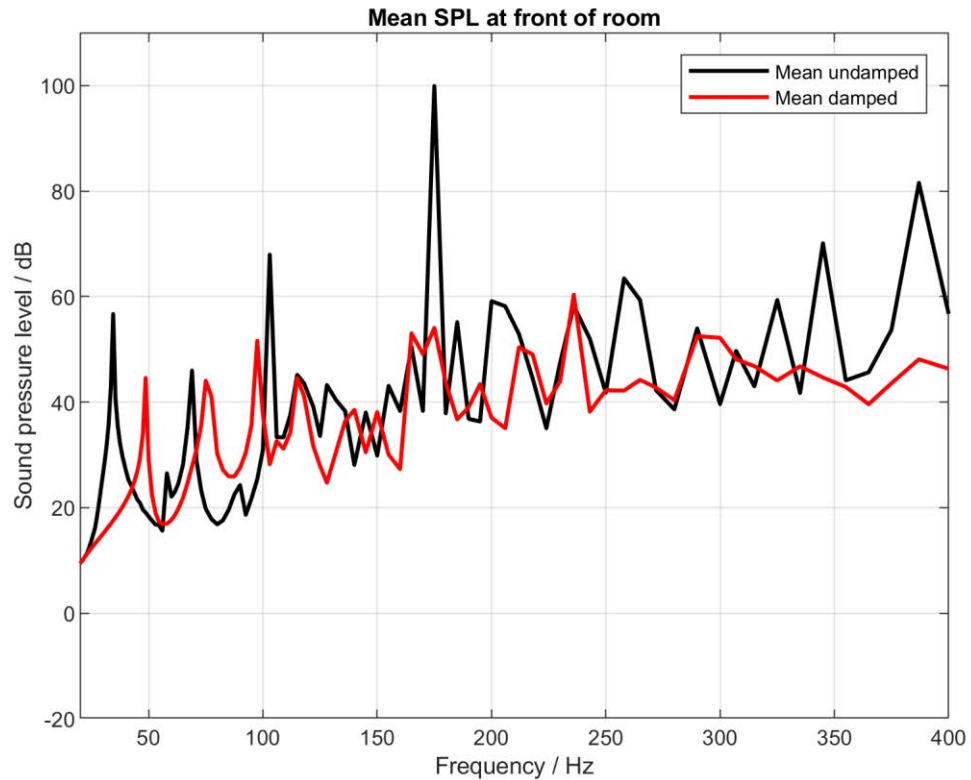
Figure 59. Average frequency response in front section for undamped (black) and damped (red) state

The same is done for the other optimal configurations for flattening the response in the center and rear sections of the room and may be seen in the following figures. In every case the same behavior may be seen. The location and amplitude of the strongest modes are shifted and decreased. A theoretical consideration of the governing equations allows us to more clearly understand why this happens.
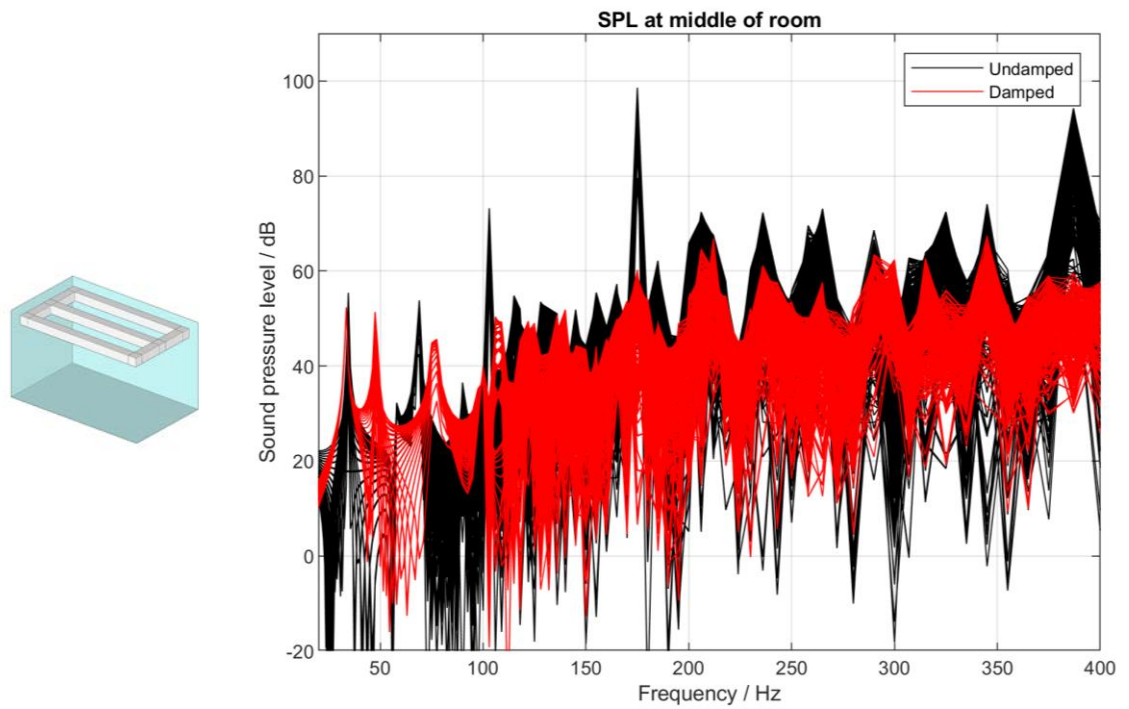
Figure 60. All frequency responses in middle section of room in undamped (black) and damped (red) states
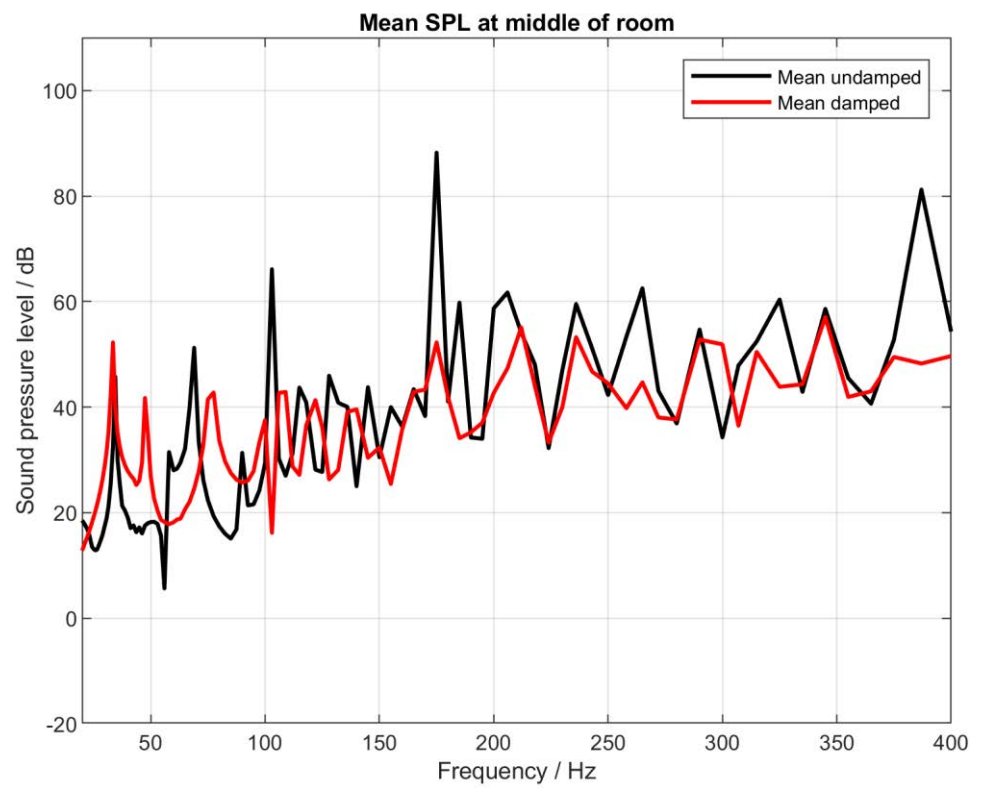
Figure 61. Average frequency response in middle section for undamped (black) and damped (red) state
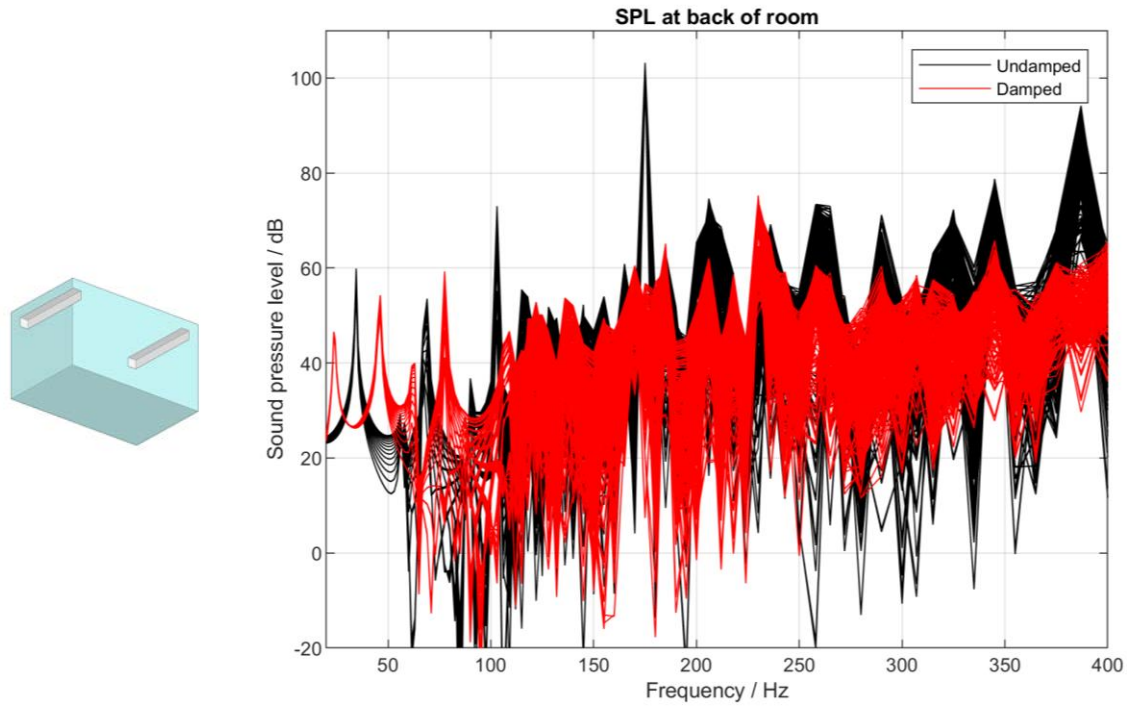
Figure 62. All frequency responses in back section of room in undamped (black) and damped (red) states
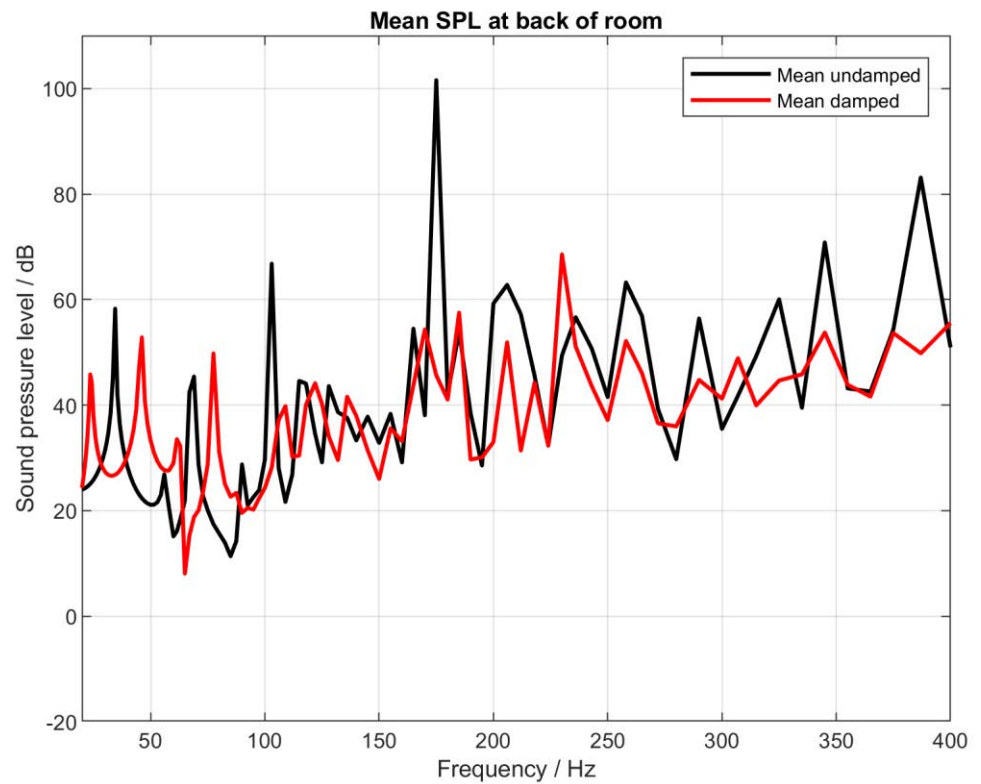
Figure 63. Average frequency response in back section for undamped (black) and damped (red) state

First, the natural frequencies of an undamped rectangular enclosure are given by:

$$f_{m,n,l} = \frac{c}{2} \sqrt{\frac{m^2}{L_x^2} + \frac{n^2}{L_y^2} + \frac{l^2}{L_z^2}}, \qquad (4.4.1)$$

or for the wavenumber

$$k_{m,n,l} = \sqrt{\left(\frac{m\pi}{L_x}\right)^2 + \left(\frac{n\pi}{L_y}\right)^2 + \left(\frac{l\pi}{L_z}\right)^2} \qquad (4.4.2)$$

where m, n, and l are the mode indices, and L_x, Ly, and L_z are the dimensions of the room.

As may obviously be seen here, the dependencies of the wave number here are either positive integers or room dimensions, which may only result in a real and positive wave number.

Beginning by expressing the 3-dimensional wave equation (based on Kleiner and Tichy, 2014, chap. 2)

$$\Delta p - \frac{1}{c^2} \frac{\partial^2 p}{\partial t^2} = 0 \qquad (4.4.3)$$

in a single x-direction, we obtain

$$\frac{\partial^2 p}{\partial x^2} - \frac{1}{c^2} \frac{\partial^2 p}{\partial t^2} = 0. \qquad (4.4.4)$$

A separation of variables leads to the equation

$$\frac{1}{X(x)} \frac{d^2 X(x)}{dx^2} = \frac{1}{c^2} \frac{d^2 T(t)}{dt^2} \qquad (4.4.5)$$

where $X(x)$ is the x-component spatial sound pressure, and $T(t)$ is the time component.

The above equation may be expressed in terms of its wavenumber with

$$-\overline{k}_x^2 = -\left(\frac{\omega + j\delta}{c}\right)^2 \qquad (4.4.6)$$

which is obviously complex, with δ being the damping factor, allowing for the calculation of losses. Already here we may see the role the damping factor plays in the resulting frequency values in the wavenumber solutions to the 1D wave equation.

The wavenumber with damping, may be expressed as

$$\overline{k}_x = \beta_x + j\alpha_x. \qquad (4.4.7)$$

When solved numerically with the finite element method, the same coefficients give the damping ratio

$$\zeta = \frac{\alpha}{2\omega_i} + \frac{\beta}{2} \qquad (4.4.8)$$

i being the mode index, resulting by solving the damping matrix

$$\mathbf{C} = \alpha\mathbf{M} + \beta\mathbf{K}. \qquad (4.4.9)$$

(Multiphysics Cyclopedia, Mode Superposition, 2018)

Analytically and back to one dimension, the harmonic function that expresses the function of the complex wave number is the transcendental equation containing the damping ratio

$$e^{jk_xL_x} = \pm\frac{k - k_x\zeta_x}{k + k_x\zeta_x} \qquad (4.4.10)$$

the solution for which, may be found numerically as stated above or by observing graphically the function

$$\tan(u) = j\frac{2u\zeta_x}{kL_x} \qquad (4.4.11)$$

or

$$\tan(u) = j\frac{kL_x}{2u\zeta_x} \qquad (4.4.12)$$

with $u = \frac{1}{2}k_xL\_x$.

Calculating the frequency response at a given position r, including the source term Q which exists at point r_0, at the frequency (wave number) k, we use the expression

$$p(r, k) = -jk\rho_0 c \frac{Q}{V} \sum_{N=0}^{\infty} \frac{\Psi_N(r_0)\Psi_N(r)}{\Lambda_N(k^2 - k_N^2)} \qquad (4.4.12)$$

where, again,

k_N is the wave number of the mode *N*, and

k is the wave number of the source.

$\Psi_N(r_0)$ is the eigenfunction evaluated at the source point r_0, while $\Psi_N(r)$ is the same function evaluated at the receiver point.

V is of course the room volume.

What becomes clear here is the dependency of the pressure at the receiver point on the term $k^2 - k_N^2$. The pressure approaches a maximum the closer k and k_N are in value, while

$$k_N = k^2 - \frac{\omega_N}{c} + j\frac{\delta_N}{c} = \beta_x + j\alpha_x \qquad (4.4.13)$$

and

$$k^2 - \overline{k}_N^2 = k^2 - \left(\frac{\omega_N}{c}\right)^2 - j2\frac{\omega_N}{c}\frac{\delta_N}{c} - \left(\frac{\delta_N}{c}\right)^2. \qquad (4.4.14)$$

Stated otherwise,

$$\overline{k}_N = \sqrt{\left(\frac{\omega_N}{c}\right)^2 - j2\frac{\omega_N}{c}\frac{\delta_N}{c} - \left(\frac{\delta_N}{c}\right)^2}. \qquad (4.4.15)$$

Finally, we can see the specific effect the damping factor, has on the frequency of the *N*th mode wave number, and the resulting pressure at sample point r within the room. Stated very briefly, an increase in the damping factor of a specific mode results in an increase in the frequency of that mode.

Going back to the image plots in the results section, one result which seems to stand out is the polarization of the room when damping is used in the four vertical edges (see Figure 47). While the frequency response at the front part of the room

was greatly improved, the standard deviation in the back section became much worse. If the frequency responses within both sections there are compared, as in Figure 64, we see a significant decrease in SPL of the minima between modal peaks. This seems to indicate that the deformation of the modal shapes caused by damping may result in a spatial shift in their respective minima, ultimately making it more difficult to optimize the entire space without negatively affecting the character of the response in certain parts of the room.
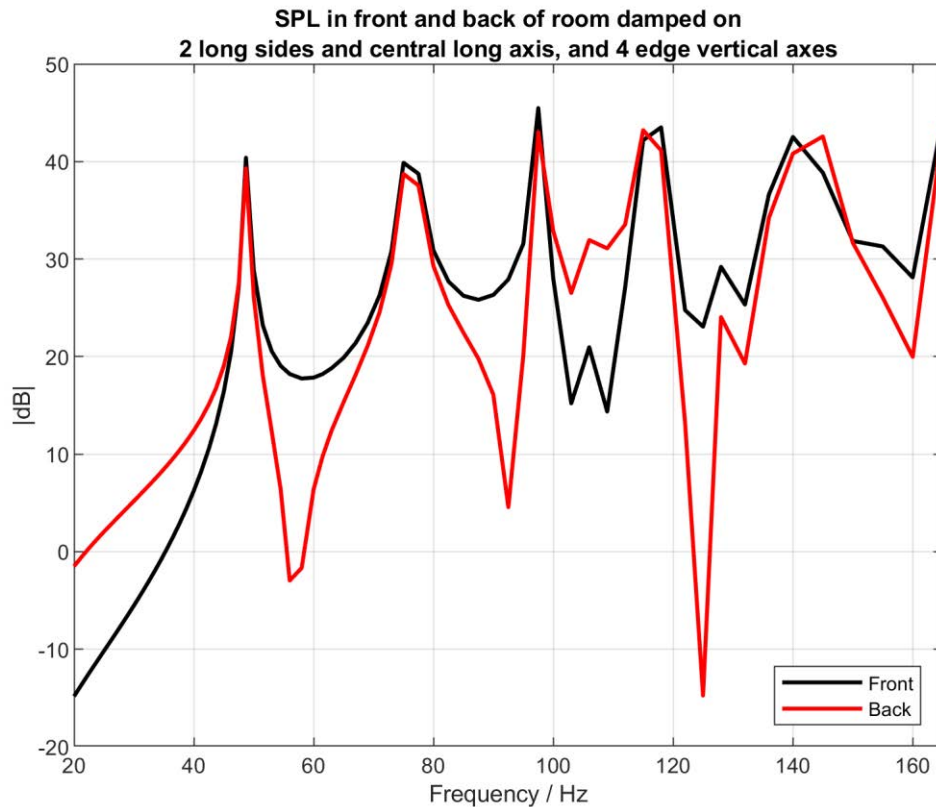
Figure 64. Frequency response in front (black) of damped room compared to back part of damped room (red). Responses taken along center axis approximately 50 cm from closest wall.

Finally, a succinct way of quantifying the statistical results of the study is to look at the percent change in frequency content included in the mean range of sound pressure levels between the undamped and damped states of within each section of the room which have been optimized with one of the absorber configurations.

In order to assess this, the standard deviation at each microphone position in each section was calculated and both added and subtracted from the arithmetic mean of all the frequency responses to create a range of standard deviation for

all frequencies and positions. The resulting frequency range is therefore frequency dependent. By evaluating the total number of SPL calculations resting within the defined range and dividing this number with the total number of points, a percentage could be obtained indicating the number of amplitudes contained within the frequency dependent average range.

In the undamped front part of the room 16.3 dB contains 79% of the amplitudes, versus the damped room in which 13.5 dB contains 75.6% of the amplitudes;

In the undamped middle part of the room 15.6 dB contains 79.2% of the amplitudes, while in the damped room 10.1 dB contains 71% of the amplitudes;

And in the undamped back part of the room 10.2 dB contains 73.1% of the amplitudes while in the damped room 8.8 dB contains 72.4% of the amplitudes on average, and within the frequency range of 20 to 165 Hz. The method described above has been borrowed from Kleiner and Tichy, though adapted by calculating the standard deviation as a frequency dependent and spatially independent function, as opposed to spatially and frequency independent as described in section 2.5 of *Acoustics in Small Rooms.*

	Undamped front	Damped front
Average range [dB]	16.3	13.5
Percent of amplitudes	79%	75.6%

	Undamped middle	Damped middle
Average range [dB]	15.6	10.1
Percent of amplitudes	79.2%	71%

	Undamped back	Damped back
Average range [dB]	10.2	8.8
Percent of amplitudes	73.1%	72.4%

Figure 65. Percent of frequency amplitudes contained within an average range of amplitudes for each section of the room

5. Conclusion

Using various methods, the results of this study have shown both empirically and theoretically that the BAT is an effective broadband absorber module, whose construction design takes advantage of two physical damping mechanisms which allow it to absorb with high strength ($.5 < \alpha < .91$) between 63 and 500 Hz, as well as moderate strength ($.3 < \alpha < .5$) between 500 and 4000 Hz. The agreement between the analytical models for membrane or plate resonator and perforated plate with porous damping and the empirical and numerical results confirm initial suppositions about the functionality of the BAT. The simulations have shown that when implemented in small to medium sized rooms, the modules shift the resonant frequencies of the space and decrease the amplitudes at which the room resonates, minimizing the standard deviation of frequency responses over significant portions of the room. The attenuation of the amplitudes of room modes, as seen in the spatial plots of the standard deviation of the frequency responses is directly influenced by the amount of absorption implemented in the space and the configuration of absorber modules within the room geometry, as shown in the results section. The general agreement between the numerical model of the surface impedance of the BAT and the analytical description and the measurements also show that the finite element method is a reliable tool for modelling boundary conditions necessary for simulating the sound field in architectural spaces within certain frequency range and for rooms with not too great a volume.

Considering the technical difficulties of producing a broadband absorber module which does not overly damp mid-range and higher frequencies (Dance and Van Buuren, 2013) the broadband absorber trap fills a void in the absorber mechanisms available at the moment, and appears to be a highly effective tool for increasing the acoustic quality of listening rooms and production rooms. As discussed in the introduction, this study addresses both a lack in surface impedance modelling method examples and low-frequency room studies conducted with the finite element method utilizing realistic boundary conditions. Additionally, this study uses a range of statistical frequency analysis methods, highlighting the necessity to complement frequency analyses with spatially dependent calculations in order to obtain a more complete understanding of the

modal behavior in the space. With validation through empirical comparison, the simulation method may also prove to be an effective planning tool for either new listening rooms or optimizing the acoustics in already existing spaces. Limitations of this study mainly rest in the fact that an absorber module with the exact dimensions of the BAT could not be tested in the impedance canal for a direct comparison. Additionally, the computation costs of the finite element method strongly limited the parametrization of the study, which could have helped in finding the optimum absorber placement configuration which both decreases the standard deviation over the largest possible area and simultaneously increases the modal density within a defined frequency range. As is often an issue in FEM, the frequency range and frequency resolution of the study was also significantly limited by the computation times per configuration, many of which had to be simulated multiple times during the prototyping phase. Finally, a direct comparison between room response measurements in a room outfitted with a set of BAT modules and a computational model would help to validate the described method as a planning tool.

There are various questions and opportunities for further research which arise as a result of this study. The first and more practically relevant exercise could be the development of an automated optimization module based on a set of frequency, spatial, and temporal cost variables for the efficient computation of the desired sound field. This would hinge on the availability of computational resources and software.

The other line of reasoning leads to a more theoretical question regarding changes to the nature of the sound field in which the BAT, understood as a resonant cavity, is implemented. Since the BAT modules are not, by stricter geometrical definition, installed *as* boundaries to the sound field within the room, and namely implemented as damping cavities fully enclosed by the transmission medium of the larger geometrical cavity, an interesting theoretical study could be the development of an analytical model for predicting the modal behavior of rectangular rooms containing smaller damping enclosures or cavities. The BAT seems to change the entire set of possible mode-shape, frequency, and amplitude combinations at which the room as LTI system may resonate, judging by the radical change in modal density shown in the simulations. Developing this

conjecture into a practical question may have praxis-oriented relevance as well, since, as we know, architectural spaces are not simply shells filled with air, but rather boundaries which contain additional shells or boundaries, or resonant cavities containing cavities which act as resonant structures. This could also be the topic of a more rigorous numerical study.

Bibliography

Antonio, P.D. and Cox, T.J., 2017. Acoustic Absorbers and Diffusers Theory.

Aretz, M., 2012. Combined wave and ray based room acoustic simulations of small rooms (Vol. 12). Logos Verlag Berlin GmbH.

Bergman, D.R., 2018. Computational acoustics: Theory and implementation. John Wiley & Sons.

Bistafa, S.R., Hodgkin, M.P., Morita, W.S., Kohn, B.O. and Neto, J.J., 2012. Adaptive control of low-frequency acoustic modes in small rooms. The Open Acoustics Journal, 5(1).

Bistafa, S.R. and Morrissey, J.W., 2003. Numerical solutions of the acoustic eigenvalue equation in the rectangular room with arbitrary (uniform) wall impedances. Journal of Sound and Vibration, 263(1), pp. 205 – 218.

Calder, J., 2018, May. New research on low-frequency membrane absorbers. In Proceedings of Meetings on Acoustics 175ASA (Vol. 33, No. 1, p. 015001). Acoustical Society of America.

Cox, T.J., D'Antonio, P. and Avis, M.R., 2004. Room sizing and optimization at low frequencies. Journal of the Audio Engineering Society, 52(6), pp.640 – 651.

Cucharero, J., Hänninen, T. and Lokki, T., 2019, September. Influence of Sound-Absorbing Material Placement on Room Acoustical Parameters. In Acoustics (Vol. 1, No. 3, pp. 644 – 660). Multidisciplinary Digital Publishing Institute.

Dance, S.M. and Van Buuren, G., 2013. Effects of damping on the low-frequency acoustics of listening rooms based on an analytical model. *Journal of Sound and Vibration*, *332*(25), pp.6891 – 6904.

Delany, M.E. and Bazley, E.N., 1970. Acoustical properties of fibrous absorbent materials. *Applied acoustics= Acoustique appliqu = Angewandte Akustik*, *3*(2), pp.105 – 116.

DIN EN ISO 354 (1985). Acoustics, Measurement of sound absorption in a reverberation chamber.

DIN EN ISO 10534-1 (2001) Akustik—Bestimmung des Schallabsorptionsgrades und der Impedanz in Impedanzrohren Teil 1: Verfahren mit Stehwellenverhältnis.

DIN EN ISO 10534-2 (2001): Akustik–Bestimmung des Schallabsorptionsgrades und der Impedanz in Impedanzrohren–Teil 2: Verfahren mit Übertragungsfunktion (ISO 10 534-2: 1998). Deutsche Fassung EN ISO, 10.

DIN EN ISO 3382-2 (2009): Acoustics — Measurement of room acoustic parameters — Part 2: Reverberation time in ordinary rooms.

Fazenda, B. and Wankling, M., 2008. Optimal modal spacing and density for critical listening.

Fuchs, H.V. and Lamprecht, J., 2013. Covered broadband absorbers improving functional acoustics in communication rooms. *Applied acoustics*, *74*(1), pp.18 – 27.

Ji, J., Li, D., Li, Y. and Jing, Y., 2020. Low-frequency broadband acoustic metasurface absorbing panels. *arXiv preprint arXiv:2002.05325*

Kleiner, M. and Tichy, J., 2014. Acoustics of small rooms. CRC Press.

Kuttruff, H., 2016. Room acoustics. Crc Press.

Magalotti, R. and Cardinali, V., 2019. Building FEM low frequency room models through modal decay time measurements. In *Proceedings of the 23rd International Congress on Acoustics, Aachen, Germany* (pp. 9 – 13)

Magalotti, R. and Cardinali, V., 2018. A simulation test bench for decay times in room acoustics. In 2018 COMSOL Conference.

Meissner, M., 2005. Influence of room geometry on modal density, spatial distribution of modes and their damping. Archives of Acoustics, 30(4), p. 205.

Meissner, M., 2008. Influence of wall absorption on low-frequency dependence of reverberation time in room of irregular shape. *Applied Acoustics*, *69*(7), pp. 583 – 590.

Meissner, M., 2018. A novel method for determining optimum dimension ratios for small rectangular rooms. Archives of Acoustics, 43.

Mondet, B., Brunskog, J., Jeong, C.H. and Rindel, J.H., 2017. Retrieving complex surface impedances from statistical absorption coefficients. In Internoise 2017: 46th international congress and exposition on noise control engineering.

Mondet, B., Brunskog, J., Jeong, C.H. and Rindel, J.H., 2020. From absorption to impedance: Enhancing boundary conditions in room acoustic simulations. Applied Acoustics, 157, p.106884.

Moser, M., Engineering acoustics: an introduction to noise control. 2009.

Multiphysics Cyclopedia, 2018, *Mode Superposition,* Comsol Inc., viewed Aug.-Oct. 2020, <https://www.comsol.com/multiphysics/mode-superposition?parent=structural-mechanics-0182-222>

Multiphysics Cyclopedia, 2018, *Eigenfrequency Analysis*, Comsol Inc., viewed Aug.-Oct. 2020, <https://www.comsol.com/multiphysics/eigenfrequency-analysis>

Pietrzyk, A. and Kleiner, M., 1997, March. The application of the finite-element method to the prediction of soundfields of small rooms at low frequencies. In Audio Engineering Society Convention 102. Audio Engineering Society.

Prislan, R., Veble, G. and Svenšek, D., 2016. Ray-trace modeling of acoustic Green's function based on the semiclassical (eikonal) approximation. The Journal of the Acoustical Society of America, 140(4), pp. 2695 – 2702.

Prislan, R. and Svenšek, D., 2017. Ray-tracing semiclassical low frequency acoustic modeling with local and extended reaction boundaries. arXiv preprint arXiv:1705.03825

Rindel, J.H., 2011. An impedance model for estimating the complex pressure reflection factor. In Forum Acusticum (Vol. 2011).

Rindel, J.H., 2015. Modal energy analysis of nearly rectangular rooms at low frequencies. Acta Acustica united with Acustica, 101(6), pp.1211 – 1121.

Sevastiadis, C., Kalliris, G. and Papanikolaou, G., 2010. Investigation of low-frequency sound colouration treatments in small rooms by means of finite element analysis. International Journal of Acoustics and Vibration, 15(3), p.128.

Smits, J.M.A. and Kosten, C.W., 1951. Sound absorption by slit resonators. Acta Acustica united with Acustica, 1(3), pp. 114 – 122.

Appendix: Complete set of room simulation results

The following set of results is the complete set of image plots generated by damping the room model shown with the model configuration used to calculate it. The image plot shows the standard deviation of the frequency response in dB at each point in the sampling array at height of 1.2 m. A lower standard deviation, given in dB and shown by increasingly darker shades of blue, represents a flatter frequency response at that specific point in the space which corresponds to the decrease in room mode amplitudes calculated from the simulated absorber configuration shown to the left of the plot.

Standard deviation of frequency response in room, damped on long central axis

Standard deviation of frequency response in room, damped on 2 long sides

Standard deviation of frequency response in room, damped on 2 long sides and long central axis

Standard deviation of frequency response in room, damped on central short axis

Standard deviation of frequency response in room, damped on 2 short sides

Standard deviation of frequency response in room, damped on central short axis and two short sides

Standard deviation of frequency response in room, damped on 2 short sides and long central axis

Standard deviation of frequency response in room, damped on central short and long axis

Standard deviation of frequency response in room, damped on central short axis and two long sides

Standard deviation of frequency response in room, damped on 2 short and 2 long sides

Standard deviation of frequency response in room, damped on 2 short and 2 long sides, and long central axis

Standard deviation of frequency response in room, damped on 2 short and long sides, and central short axis

Standard deviation of frequency response in room,
damped on 2 short and long sides, central long and short axes

Standard deviation of frequency response in room,
damped on 4 edge vertical axes

Standard deviation of frequency response in room, damped on 2 long sides and 4 edge vertical axes

Standard deviation of frequency response in room, damped on 2 short sides and central long axis, and 4 edge vertical axes

Standard deviation of frequency response in room, damped on 2 short sides and 4 edge vertical axes

Standard deviation of frequency response in room, damped on 2 short and long sides, and 4 edge vertical axes

Standard deviation of frequency response in room,
damped on 2 long sides and central long axis, and 4 edge vertical axes

Standard deviation of frequency response in room,
damped on 2 short and 2 long sides, 2 central axes, and 4 edge vertical axes